Master's Thesis

Enhancement of polymer electrolyte fuel cell tolerance to CO by combination of different mitigation methods

Taneli Rajala

21 November 2013

University of Helsinki
Department of Chemistry
Laboratory of Physical Chemistry

Faculty	Department
Faculty of Science	Department of Chemistry

Author
Taneli Rajala

Title
Enhancement of polymer electrolyte fuel cell tolerance to CO by combination of different mitigation methods

Subject
Physical Chemistry

Level	Month and year	Number of pages
Master's Thesis	November 2013	52

Abstract

Enhancement of polymer electrolyte fuel cell tolerance to CO impurities would allow the use of lower quality H_2, thus reducing the costs without compromising fuel cell performance. In this work, the effect of CO is mitigated by combining different methods, including air bleed, varying the anode flow rate and using a state-of-the-art Pt−Ru catalyst at two operating temperatures.

The tolerance was investigated by feeding a novel arrangement of segmented cells with H_2 containing CO less than 20 ppm. Anode exhaust gas was constantly analysed using a gas chromatograph.

It was discovered that increasing the volumetric flow rate of H_2 and especially utilising Ru in the catalyst enhance the CO tolerance. When applying the air bleed, an O_2/CO molar ratio of at least 117 was required to stop the poisoning with a Pt catalyst. Approximately a fifth of the air bleed needed with Pt was enough with Pt−Ru. The results also suggest that when applying air bleed at elevated temperatures, it is beneficial to lower the cell temperature for the duration of the air bleed.

Keywords
Polymer electrolyte fuel cell, hydrogen quality, carbon monoxide, air bleed

Where deposited

Additional information

Contents

1   Introduction

Let us imagine how the appearance of our industrial cities would change if energy was produced efficiently by electrochemical methods – no more smoke, no more soot! This could be a bold scene from the daydream of today's environmentalist. In fact, it was originally envisaged by Wilhelm Ostwald, a Nobel laureate in chemistry, who realised the revolutionary potential of fuel cells already in 1894 [1]. The present energy and climate crisis reminds us of the little interest Ostwald's views were treated with. After a century of nonchalant squander people are finally becoming ready to share his vision.

In the past, fuel cells have often been dwarfed by oil industry due to technical challenges and high costs. However, it can be argued that the Space Race initiated the upcoming breakthrough of fuel cell technology in the mid-to-late 20th century. Greater efficiency, eco-friendly operation, and the high energy density of H_2 have among other things paved the way for fuel cells as power sources in industry and consumer market.

Major technical challenges of polymer electrolyte fuel cells (PEMFCs) have been tackled but more research and development should still be focused on at least increasing the long-term durability and reducing the total cost of ownership [2–4]. Fuel impurities in reformate hydrogen affect the both and overall performance besides.

The most researched poisoning agent in reformate fuel is CO. Efficient mitigation of CO poisoning would inhibit the damage to the cell and allow higher levels of the contaminant in H_2 for both stationary and transportation applications. Lower requirements for the H_2 purity would cut the costs of both purification and quality assurance. The present work addresses the mitigation of CO poisoning by combining different methods.

2 Fuel cells

2.1 Brief overview

Fuel cells are electrochemical converters that generate electricity by means of a chemical reaction between a fuel and its oxidant. During the course of the reaction heat is generated and water is formed as a product. Carbon dioxide is also produced when using carbon-containing fuels.

A single fuel cell is a simple galvanic cell. Fuel is oxidised at the anode and oxygen is reduced at the cathode. The electrodes are separated by an ion-conducting electrolyte. To prevent short circuits and maximise electrical work, an ideal electrolyte is impermeable to electrons and the fuel as such. For a hydrogen fuel cell, anode and cathode reactions, respectively, are

$$H_2 \longrightarrow 2\,H^+ + 2\,e^- \tag{1}$$

$$O_2 + 4\,H^+ + 4\,e^- \longrightarrow 2\,H_2O \tag{2}$$
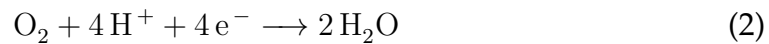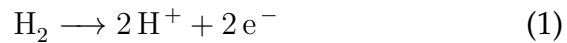
When a fuel cell is connected to an electrical circuit, a potential difference* is achieved between the electrodes. The static electric field $\mathbf{E}$ produced determines the force $\mathbf{F}$ experienced by the electrons liberated from the fuel as follows

$$\mathbf{F} = q\mathbf{E} \tag{3}$$

By vector analysis, it can be easily shown that the curl of a static field $\mathbf{E}$ vanishes, which is why the field can be written as a function of the prevailing potential ϕ [6]

$$\mathbf{E} = -\nabla\phi \tag{4}$$

---

*Strictly speaking, a difference in electrochemical potential $\bar{\mu}_i = \mu_i + q_i\phi$, where i refers to the charge carrier, is formed [5]. The first term on the right-hand side denotes chemical potential $\mu_i = \mu_i^\circ + RT\ln(a_i)$ and the second the electrical correspondent. When attempting to find an expression for the electrical work drawn from the circuit, the chemical environment of the charge can be neglected, that is, chemical activities of $a_i = 1$ can be assumed. Then, apparently, one is able to derive electrical work from plain electrostatics.

Let us consider a charge q moving from the anodic potential ϕ_a to the cathodic one ϕ_c under the static field expressed above. By the physical definition of work, the relation between work W done by the field on the charge and the voltage V between the electrodes is given by

$$W = \int_a^c \mathbf{F} \cdot d\mathbf{s} = -q \int_a^c \nabla \phi \cdot d\mathbf{s} = -q(\phi_c - \phi_a) = -qV \tag{5}$$

Usually, this maximum electrical work is identified with the change in Gibbs free energy, ΔG. For a mole of charges, one can write

$$\Delta G = -zFV \tag{6}$$

where z is the number of exchanged electrons per mole of the reactant in the overall reaction and F is the Faraday constant.

2.2 Efficiency

2.2.1 Ideal efficiency

As characteristic of any engine transforming energy into useful work, there is a theoretical efficiency limit for fuel cells. Even in the ideal case of assuming zero heat losses, part of the energy difference between the reactants and products is inevitably out of reach due to uncontrollable entropy changes.

To attain an expression for the thermal efficiency of a system, we compare the exploitable energy with the total energy input. By introducing a basic thermodynamic relation $G \equiv H - TS$, the efficiency η_{id} of an ideal electrochemical converter can be formulated as

$$\eta_{\text{id}} = \frac{\Delta_{\text{r}} G}{\Delta_{\text{r}} H} = 1 - \frac{T \Delta_{\text{r}} S}{\Delta_{\text{r}} H} \tag{7}$$

where T is temperature, $\Delta_{\text{r}} H$ is the enthalpy and $\Delta_{\text{r}} S$ the entropy change of the reaction.

From equation (7), it is obvious that for every combustion reaction of negative entropy, $\eta_{\text{id}} < 1$. But what about a combustion reaction of positive

entropy? In principle, ideal efficiencies over 100% would be possible. Typically they are in the range of 80% to 95%, but for instance, for the combustion of carbon to carbon monoxide, $C\,(s) + \frac{1}{2}O_2\,(g) \longrightarrow CO\,(g)$, the ideal efficiency amounts to 124% [7].

This violation of the laws of thermodynamics is illusory since the additional electrical energy is absorbed from the surroundings as heat. To avoid misunderstandings, Lutz et al. have suggested adding a heat term $-T\Delta_r S$ to the nominator in equation (7) for positive entropies of reaction [8].

2.2.2 Real efficiency

The actual efficiency of the cell is not the one expressed in equation (7). In practice, when current is drawn from the cell, the voltage starts to drop from the open circuit value (OCV) due to various losses such as activation, ohmic, and mass transfer overpotentials. In terms of efficiency, this behavior can be simply encapsulated by

$$\eta_v = \frac{V}{V_{ocv}} \tag{8}$$

where η_v is voltage efficiency and V_{ocv} denotes open circuit voltage.

As electrolytes always diverge from ideal behaviour, some electrical leakage and fuel crossover through the electrolyte have to be included in efficiency considerations. In order to ensure sufficient fuel concentration in every part of the cell, reactants are fed in stoichiometries over one. The stoichiometric coefficient, λ_i, is defined as the amount of reactant i supplied divided by its theoretical consumption. The stoichiometric coefficient is, in effect, the reciprocal of faradaic efficiency η_f. Using Faraday's laws of electrolysis gives

$$\lambda_i \equiv \frac{1}{\eta_f} = \frac{zF\dot{n}_i}{I} \tag{9}$$

where $\dot{n}_i$ is the molar flow rate of the fuel and I is the current drawn.

By summing up the implications of equations (6), (7), (8), and (9) we get

$$\eta_{\text{tot}} = \eta_{\text{id}}\eta_{\text{v}}\eta_{\text{f}} = \frac{-VI}{\dot{n}_{\text{i}}\Delta_{\text{r}}H} \tag{10}$$

which is the real efficiency of an electrochemical converter. [7]

2.2.3 The myth about superior efficiency

Greater efficiency is one striking advantage of fuel cells over heat engines such as internal combustion engines in cars. It should be noted, though, that this is not because of some thermodynamic prerogative inherent to fuel cells. It is only a popular fallacy that since in fuel cells the energy gained depends solely on electron transfer, they are disengaged from Carnot efficiency limits distinctive to conventional heat engines (see for example [9,10]).

Carnot efficiency is a manifestation of the second law of thermodynamics from which there is nothing to exempt fuel cells [11]. Lutz et al. have considered an ideal heat engine using the combustion reaction of the fuel cell as its heat input, eventually ending up with equation (7) for the efficiency [8].

Of course, a fuel cell is not a heat engine. What is underlined here is that both are equally constrained in terms of maximum efficiency. Nevertheless, in heat engines, the moving fluid requires high operating temperatures. This results in losses not characteristic of fuel cells, making heat engines in practice less efficient. [8,12]

2.3 Polymer electrolyte fuel cell

Fuel cells are typically classified according to electrolyte type, the fuel chosen, or operating temperature [10]. Electrolyte categories include, for example, solid oxide, alkaline, and polymer materials. This thesis focuses on a polymer electrolyte membrane fuel cell (PEMFC) fed with hydrogen and operated at low temperatures.

The heart of the polymer fuel cell is a membrane electrode assembly (MEA). It comprises a layered configuration of a polymer electrolyte membrane and porous electrodes surrounded by a gas diffusion layer (GDL) on either side. The MEA is sandwiched between a pair of flow field plates, that

together with the GDLs, enable an even distribution of reactants to the electrodes. The plates also convey products, excess reactants, and heat out of the system and transmit electrical current via current collectors to an external circuit. In the following, the MEA components will be introduced.

2.3.1 Proton exchange membrane

At the anode, hydrogen molecules are oxidised to ions which are needed in oxygen reduction at the cathode. The membrane between them ensures electronic insulation of the electrodes and prevents reactant gases from mixing with each other. In order to minimise ohmic losses it should also exhibit the highest proton conductivity possible. For this purpose, DuPont developed Nafion, a perfluorosulfonate ionomer (PFSI), which already penetrated the membrane market in the late 1960s. PFSI-based membranes are still regarded as standard [9]. Smitha et al. [13] have reviewed alternative solid polymer electrolytes.

Nafion is a graft copolymer. An earlier discovery by DuPont, polytetrafluoroethylene (PTFE), better known as Teflon, serves as the backbone of the polymer. Strong bonds between carbon and fluorine make the structure resistant to most chemical degradation. Side chains branching from the backbone consist of a varying number of perfluorosulfonate ionomers whose polar ends are capable of absorbing sufficient amounts of water for proton transport.

Water management

Water management is critical to the overall cell performance. On the one hand, one must avoid flooding. Excess water tends to block the pores of the electrodes and the GDLs or even accumulate in the flow channel, thus preventing the reactants from reaching the electrochemically active catalyst area. On the other hand, if the moisture level is too low, proton conductivity falls and the membrane may sustain irreversible damage.

What makes matters more complicated is that the water content is rarely even throughout the cell. Especially at high current densities the anode side may dry out due to hydrogen ions pulling extra water molecules with them. This electroosmotic drag together with water generation at the cathode establish a substantial concentration gradient across the membrane. Especially for thin membranes, this results in back-diffusion of water to

6

the anode, which is supported by Fick's first law of diffusion and experimental research [14].

In addition to optimising the membrane thickness, one can facilitate water management by humidifying the reactants and adjusting temperature and pressure so as to prevent water from evaporating. The demand of Nafion for liquid water sets the upper limit of operating temperature range close to 100 °C. Water management has been vigorously studied and a good review of the topic is given by Dai et al. [15].

2.3.2 Electrodes

The electrode is where the electrochemical reaction takes place. In hydrogen fuel cell reactions, there are three participants: electrons, protons, and gases. This implicates a three-phase boundary where all reactants may come together.

The electrode consists of tiny catalyst particles dispersed on mesoporous carbon powder that is embedded in the ionomer membrane. Close contact between the membrane and the catalyst is necessary for the protons to propagate to the reaction site. The porous structure aids gas diffusion and the carbon support conducts electrons to the desired destination. [16,17]

2.3.3 Gas diffusion layer

The gas diffusion layer allows even distribution of reactants to catalyst surface and promotes the removal of both water from the cathode and heat from the electrochemical reaction site. The GDL also electrically connects the electrodes to the flow field plates and provides mechanical stability to the MEA.

At present, commonly used GDL materials are porous carbon fibers mixed with some hydrophobic PTFE to avoid flooding. In dual-layer structures, this macroporous surface is connected with the catalyst layer by a thinner microporous layer of PTFE embedded in carbon powder. Readers more interested in recent developments of GDL material design and its role in gas diffusion and water management are referred to a review by Park et al. [18].

2.4 CO poisoning

There are several fuel contaminants that even at trace levels undermine the performance of a PEMFC. The most significant of these include at least CO, H_2S, and NH_3 [19]. While damage caused by the former is reversible, losses due to H_2S and NH_3 are usually more slowly recovered. Additionally, the longer the exposure time, the more severe the damage. [20,21]

Ammonia as a base is suggested to react with protons, replacing H^+ with NH_4^+, thus significantly decreasing the proton conductivity of the membrane [21]. Other impurities typically reduce the performance by either displacing adsorbed hydrogen molecules from the catalyst surface or by blocking available sites.

H_2S is considered an even more severe poisoning agent for platinum catalysts than ammonia, although it can be made to desorb more easily by electrochemical methods [22, 23]. H_2S bonds strongly to both platinum and ruthenium, which is why the presence of the latter does not increase the tolerance as is the case with CO poisonings [22]. For the time being, no practical solutions to H_2S nor NH_3 poisoning are available for system level applications.

CO_2 can also result in poisoning but its degradative effect seems to be based on the formation of CO by either reverse water gas shift reaction or the electrochemical correspondent with hydrogen ions on platinum surface [20,24]. This surface reaction is significantly quenched by the addition of ruthenium to the catalyst. Carbon dioxide itself adsorbs on platinum rather loosely and reduces the performance mainly by diluting the fuel. However, due to the formation of CO, high levels of CO_2 in the fuel can result in moderate poisoning. [24]

CO is the most pernicious poisoning agent and the most researched one. In the following, CO poisoning will be examined more closely.

2.4.1 Why there is CO in H_2 fuel

Although renewable energy solutions have been around for some time, and even longer under vigorous research, an overwhelming majority of industrial hydrogen is still produced from fossil fuels [25]. A common denominator of all carbon-based hydrogen production is the impurity of the final product. This proves quite troublesome in the case of PEMFCs,

which are highly intolerant[†] of CO.

Steam reforming of natural gas along with partial oxidation and autothermal reforming are one of the most feasible and cost-effective procedures in the large-scale manufacture of hydrogen. Natural gas is primarily methane, featuring a mixture of hydrocarbons with low boiling points and components of air in minor amounts. In steam reforming, methane is mixed with steam at temperatures above 700 °C in the presence of a catalyst to yield H_2 and CO. Most of the latter is subsequently removed via the water-gas shift (WGS) reaction presented in equation (12). These steps may be summarised as [9]

$$CH_4 + H_2O \xrightarrow[\text{700–1100°C}]{\text{Ni}} CO + 3\,H_2 \tag{11}$$

$$CO + H_2O \xrightarrow[\text{2. CuO/ZnO at 200–250°C}]{\text{1. Fe}_2\text{O}_3/\text{CrO}_3 \text{ at 400–500°C}} CO_2 + H_2 \tag{12}$$
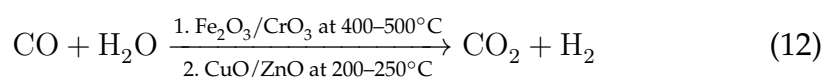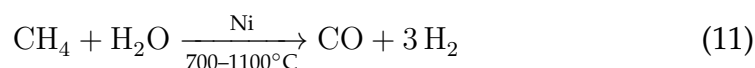
One technical challenge here is that the former reaction is moderately endothermic and the latter slightly exothermic. Therefore, for the WGS reaction to really take place to the desired extent, one has to complement the steam reforming system by one or two shift reactors. Gas products from the steam reformer are cooled before passing them to the shift conversion, still resulting in CO concentrations of thousands of ppms.

2.4.2 How to diminish the impurity level

After reaching the level of thousands of ppms of CO, further purification is required for PEMFC use. Methanation and pressure swing adsorption (PSA) can be cited as two commonly applied procedures. Methanation includes reaction (11) in the opposite direction at lower temperatures with appropriate catalysts. It obviously has the drawback of consuming a bit of hydrogen as well as diluting the reformed product with methane. Nevertheless, this clean-up results in CO levels of less than 10 ppm. [9]

In PSA, the impurities are separated from the product by means of diverging affinities for solid adsorbents such as zeolites. The product from shift

---

[†]In this context, the cell being *tolerant* usually implies its capability of electrooxidising hydrogen at certain current densities, suffering no more than a voltage loss of tens of millivolts [26]. The definition includes that the drop is permitted to happen only within a relevant time scale whose extent depends on the application.

reactors is passed through a pressurised vessel lined with adsorbent material to which impurities cling, enriching the outcoming gas with hydrogen. The adsorbent bed can be regenerated by depressurising the vessel, leading the contaminants out of the system, and then by purging the bed with hydrogen. After that, the clean-up cycle can be repeated. [27, 28]

These purification methods for the reformer product are a great source of expense, which is why WGS reaction promoted by bacteria may attract particular interest. This biological approach allows ambient temperatures, significantly increasing the equilibrium constant of the exothermic reaction (12). As to the kinetics, it is suggested that the rate-limiting step is the mass transfer of gaseous CO to the liquid bacterial suspension of the bioreactor rather than the WGS reaction therein. [29] During the course of a few days' incubation period, the ability of micro-organisms to metabolise CO develops, which later results in CO conversion close to 100%. [30]

Furthermore, one economical and practical method is the selective catalytic oxidation of CO to CO_2. For levels up to 10 000 ppm of CO, a correspondingly small amount of O_2 is enough to decrease the CO concentration to the region of 5 ppm. By applying a highly selective catalyst such as Pt/Al_2O_3, the oxidation of the 30–70% hydrogen present in the reformate remains negligible. [31]

Typically, the reformed product contains CO somewhere in the range of 10 to 100 ppm, depending on the quality demands and manufacture procedure chosen. [32] Even such CO levels tend to notably reduce PEMFC performance. Therefore, for the automotive industry, the desired CO concentration of the fuel has been set as low as 0.2 ppm. [33] However, all purity requirements of various applications may not be equally stringent. Combined heat and power production and fleet machine applications such as container handling equipment could be utilised with refinery grade hydrogen, employing the contamination mitigation presented later.

2.4.3 Mechanisms

The H_2 electrooxidation on Pt surface is often suggested to take place in two stages, according to the well-known Tafel–Volmer mechanism [34]:

$$H_2 + 2\,Pt \rightleftharpoons 2\,Pt{-}H \tag{13}$$

$$Pt{-}H \longrightarrow Pt + H^+ + e^- \tag{14}$$

10
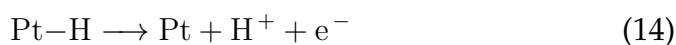
The first step, where H_2 dissociates, is rate-determining and calls for two adjacent Pt sites. The following discharge of adsorbed hydrogen is relatively rapid. If CO molecules reach the platinum surface of the catalyst, they start to adsorb onto it with greater affinity than hydrogen. CO can either displace hydrogen or bind directly to Pt, thereby blocking the active sites for the hydrogen dissociation [34]:

$$2\,Pt{-}H + 2\,CO \longrightarrow 2\,Pt{-}CO + H_2 \tag{15}$$

$$CO + Pt \rightleftharpoons Pt{-}CO \tag{16}$$

Experimental research has demonstrated that the rate of H_2 oxidation on Pt catalyst depends linearly on the bare Pt sites on the surface [35]:

$$i_{H_2/CO} = i_{H_2/CO}^{\circ}(V, T, P)[1 - \Theta_{CO}] \tag{17}$$

where $i_{H_2/CO}$ is the current density of H_2 oxidation in the presence of CO, $i_{H_2/CO}^{\circ}$ is the corresponding exchange current density, V is potential, T temperature, P pressure, and Θ_{CO} the fraction of the Pt surface that is covered by CO.

When $\Theta_{CO} > 0.8$, the oxidation current starts to deviate from the linear behaviour stated in equation (17). Full coverage is reached with CO concentrations as low as 10 ppm. [35] The lower the concentration, however, the slower the poisoning becomes [36].

If no performance failure is allowed, CO must be completely removed. For this purpose, the electrode potential can be raised in order to electrooxidise the adsorbed CO to CO_2. The oxidation proceeds via the following reactant-pair mechanism [37–39]:

$$Pt + H_2O \rightleftharpoons Pt{-}OH + H^+ + e^- \tag{18}$$

$$Pt{-}CO + Pt{-}OH \rightleftharpoons CO_2 + 2\,Pt + H^+ + e^- \tag{19}$$
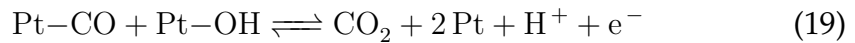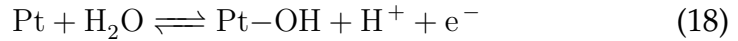
2.5 Mitigation of CO poisoning

Requirements for neater H_2 add to the costs due to more precise purification and quality assurance. Furthermore, poisoning the fuel cell causes irreversible damage to the MEA in the long run. That is why it would be optimal to be able to feed the cells with somewhat contaminated hydrogen, without exposing them to severe poisoning.

Fortunately, there is a variety of ways to alleviate the effects of CO. They are encompassed by four strategies: introducing O_2 to the anode feed, varying the catalyst composition, shifting the anode potential to electrooxidise CO, and adjusting the operating temperature and pressure. These principles will be briefly discussed in the following.

2.5.1 Effect of O_2 at the anode

It has been established that by introducing minor amounts of O_2 in the fuel stream entraining traces of CO, the detrimental agent can be eliminated [40]. Oxygen adsorbs onto the Pt catalyst and is suggested to oxidise the adsorbed CO via the Langmuir–Hinselwood mechanism [38,39]. Some of the CO may be removed by direct combustion or the WGS reaction as well. Instead of pure O_2 one often applies air. By air bleed one refers to either internal or external.

Internal air bleed

Oxygen crossover from the cathode to the anode is referred to as internal air bleed. As long as there is an oxygen concentration gradient between the cathode and the anode, this type of natural air bleed is present. There are ways of enhancing this property. With membranes thin enough ($\leq 25\ \mu$), increasing cathode backpressure serves as a mitigation method. Some of the oxygen fed in at the cathode diffuses through the membrane and oxidises CO at the anode. The higher the cathode backpressure and the thinner the membrane, the more intense is the diffusion.

Nevertheless, Wang et al. have shown that in the case of 50 ppm CO in H_2 with anode and cathode pressures of 101 and 303 kPa, respectively, internal air bleed is not alone capable of recovering the performance to the level of neat hydrogen. The alleviating effect, however, is indisputable and suggested to become more effective with increasing temperature. [41]

12

External air bleed

Because natural air bleed does not provide full protection for fuel cell poisons, but contributes anyway, one is tempted to move on to mixing air with the anode fuel feed. External air bleed is capable of almost totally recovering the cell performance, and it has also proven workable in long-term poisonings [42].

However, it is of central importance to optimise the level of O_2 fed in. Too low a level is inadequate to recover the performance, but too high a level has the disadvantage of degrading the membrane. Roughly 0.5% air bleed of the total fuel flow per each 10 ppm of CO may be enough to recover the performance [43].

While possibly a sufficient mitigation method, air bleed is not really an efficient one. Only a tiny fraction, about 10^{-4}, of the consumed oxygen actually participates in the oxidation of carbon monoxide [44]. Most of the oxygen is reduced by protons in either of the following half-reactions:

$$O_2 + 4\,H^+ + 4\,e^- \rightleftharpoons 2\,H_2O \tag{20}$$

$$O_2 + 2\,H^+ + 2\,e^- \rightleftharpoons H_2O_2 \tag{21}$$
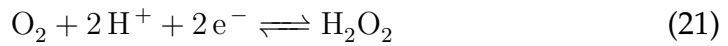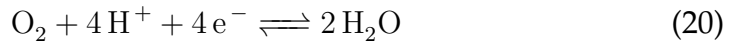
Some of the oxygen may also react exothermally with hydrogen. In principle, this can cause local fuel starvation and membrane drying, but with fully humidified gases it should have no influence on the current distribution through the cell [43].

Because of the poor selectivity for CO oxidation, oxygen must be fed in excess. Besides the undesired consumption of the fuel, additional oxygen contributes to the degradation of the MEA due to the formation of H_2O_2 through the reaction (21).

The H_2O_2 yield depends partly on the platinum monolayer coverage. If $\Theta_{CO} > 0.5$, H_2O_2 is formed at notably higher rate than when $\Theta_{CO} < 0.4$. That is because adsorbed CO effectively blocks catalyst sites for the decomposition of H_2O_2. [45] In other words, CO coverage is desired to be kept low also in view of membrane degradation.

The formation of H_2O_2 is unfortunate since it results in hydroxy and peroxy radicals ($\cdot$OH, $\cdot$OOH) that permanently degrade the PFSA polymer in Nafion [46, 47]. In long air bleed experiments, it has been demonstrated

that in the presence of too much oxygen, the degradation rate of the membrane is enhanced after several weeks of operation [48].

Pulsed external air bleed

When the CO coverage is approaching one, the CO adsorption is supposed to become slower due to increasing repulsive forces affecting each free Pt site. On the other hand, this implies that the higher the CO coverage, the faster is the desorption. Then, if the performance recovery by air bleed is faster than the poisoning by CO, the poor selectivity of O_2 to oxidise CO could be compensated by feeding the cell with only pulses of air. By periodically shutting off the air bleed, one could significantly diminish the extent of the reaction with hydrogen and its pernicious side-effects. [49,50]

2.5.2 Variation of catalyst composition

The most common electrocatalyst for hydrogen oxidation and oxygen reduction in acidic environment is platinum. The bottleneck of the two fuel cell half-reactions is the latter, having an exchange current of the order of 10^{-10}A/cm^2, whereas that of hydrogen is in the range of 10^{-3}A/cm^2 [25, 51]. Besides platinum, other noble metals such as ruthenium, palladium, gold and silver can be utilised as well. From the catalytic point of view, there are two mitigative approaches: increasing the Pt loading and using binary Pt alloys.

Increase of Pt loading

Decades ago, when PEMFC research was still in its infancy, platinum was used as much as 28 mg/cm^2. The myth of platinum being the most significant factor in cost estimates originates from the early days of PEMFCs. [9] While still costly, platinum is no longer an economic bottleneck. The development of the carbon support nanostructure since the 1990s has led to a hundredfold decrease in Pt content.

Increasing Pt loading has been shown to result in improved power generation in the presence of CO [52]. For pure H_2/air operation, the quantity of platinum needed is less for the anode than the cathode due to the more intricate reaction mechanism of oxygen reduction. In state-of-the-art MEAs,

only 0.05 mg/cm^2 may be sufficient at the anode, while the cathode loading may need to be a few times greater in order to avoid notable voltage losses [53].

To render the oxygen reduction practically advantageous, the focus should not be on increasing the catalyst loading but rather in its more efficient utilisation by maximising the reactant surface area. For this purpose, it is a common practice to finely scatter tiny platinum particles with diameters of nanometer scale on the catalyst support, generally mesoporous carbon powder. [16]

Use of binary Pt alloys

The most common alloy component besides platinum is ruthenium, but unnoble ones like molybdenum and tin are sometimes used as well. With around 100 ppm of CO, the minimum Pt$-$Ru loading needed in state-of-the-art MEAs is about 0.2 mg/cm^2 [53]. In order to decrease the loading, one should either reduce the CO content or apply other mitigation methods. As for the cathode, the impurities in hydrogen implicate no necessary changes in the catalyst composition.

Blending platinum and ruthenium together with a 1:1 atomic ratio has proved the most efficient at electrooxidising adsorbed CO. The cooperation of the two appears to be synergistic. [54] If the adsorbed CO is assumed to be linearly bonded to the catalyst layer[‡], its electrooxidation can be described by a mechanism including the formation of a Ru$-$OH surface complex [55]:

$$Ru + H_2O \rightleftharpoons Ru-OH + H^+ + e^- \tag{22}$$

$$Ru-OH + Pt-CO \rightleftharpoons CO_2 + Pt + Ru + H^+ + e^- \tag{23}$$
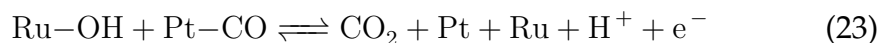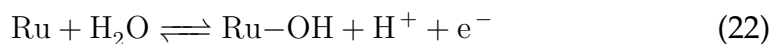
In principle, the intermediate product of this bifunctional mechanism on Pt$-$Ru could also be Pt$-$OH since it is actually more stable than Ru$-$OH. However, according to density functional calculations on cluster models, the Pt complex is less inclined to catalyse the oxidation of Pt$-$CO [56]. This trend is experimentally supported by Chung et al., who after poisoning

---

[‡]The higher the CO coverage, the greater fraction of all adsorbed CO is linearly bonded. The alternative bridge-bonding no longer manifests above coverages of 0.9. [35]

purged the cell with hydrogen, obtaining faster recovery on Pt−Ru than on pure Pt [57].

Even though Pt−Ru catalysts prove beneficial to tackling CO poisoning, they are not the end of the story. At anode potentials higher than 0.9 V vs. RHE, ruthenium starts to dissolve followed by membrane crossover and finally deposition on the cathode catalyst [58]. Not only does this degradation shorten the lifetime of the cell, but it also hinders both electrode reactions.

A remedy for the dissolution has been offered by synthesising highly stable Pt−Ru structures or, for example, by blending in stabilising agents such as silicon and titan oxides. Besides by inhibiting the anode degradation, cathode contamination could be restrained by more impermeable membranes to Ru or more Ru-tolerant electrocatalysts for the oxygen reduction. A deeper analysis of the problem and its solutions has been addressed by Antolini [59].

To avoid problems with the instability of Ru and also to diminish the dependence on Pt, one can even resort to Pd-based alloys with as low Pt content as 5%. Such Pd alloys can be comparable with Pt-based catalysts in terms of both normal hydrogen fuel cell operation and CO tolerance. For the time being, some performance loss may result due to greater particle size and thus lower active area of the Pd catalyst. However, in contrast to Pt, a push towards the development of Pd-based catalysts is given by the lower price and the greater abundance of Pd in nature. [60–62]

2.5.3 Increase in anode potential

A contaminated anode can be cleaned by raising its potential up to a zone where adsorbed CO desorbs. The threshold depends solely on the catalyst composition and structure and can be easily determined by cyclic voltammetry. For pure Pt catalysts, the potential amounts to 0.5–0.8 V vs. RHE, whereas for Pt−Ru it is only about 0.35–0.5 V. [39, 63]

Under certain conditions in galvanostatic mode, self-oxidation of the adsorbed CO can take place when the surface coverage $\Theta_{CO} \to 1$. In order to keep up the constant current, the anode potential responds by approaching higher potentials, eventually reaching the desorption threshold. This increases the fraction of free Pt sites inducing H_2 oxidation, thus decreasing the anode potential to values where CO again dominates the adsorption. As a result, the whole cycle starts from the beginning.

The intensity of self-oxidation is greatly dependent on careful optimisation of operating temperature, current density, and anode flow rate. Furthermore, it does not occur as easily on Pt as on Pt−Ru because the electrooxidation of CO includes the formation of OH_{ad}, which is more facile on Ru than Pt. [64] These stringent conditions make self-oxidation a quite rarely adopted mitigation method.

Current or voltage pulsing

Self-oxidation may not prove very efficient in enhancing CO tolerance, but it provides the basis for a more workable technique called current pulsing [65] or voltage pulsing [66]. In these methods, one controls the cell current in a predetermined scheme, thus allowing the potential to oscillate. Carrette et al. [67] have established that by current pulsing, 70% of the initial performance of the CO-contaminated cell can be restored.

The concentration of CO has no effect on the oxidation potential but it does dictate the optimum frequency of the current pulses. If the CO level is high and the waiting period between the pulses comparatively long, re-adsorption occurs resulting in inadequate mitigation. Therefore, careful optimisation has to be included when implementing these methods.

The efficiency of pulsing techniques in removing CO from the catalyst surface could be verified by similar anode exhaust gas analysis as presented in this work. In any case, shifting anode potential provides fuel cell design with more room for manoeuvre.

2.5.4   Operating temperature

Operating temperature is a parameter that affects both adsorption and diffusion, thus playing an implicit role in the methods already mentioned. It may not, therefore, be legitimate to survey it as a separate mitigation method, but its effects on fuel cell design are worthy of a brief discussion in any case.

CO adsorption on platinum is an exothermic reaction, which implies that CO coverage on platinum decreases with increasing temperature. Raising the temperature improves the kinetics of both a non-poisoned and a poisoned cell, but this relation is even more pronounced in the latter case. [68] In fact, the desorption of CO has been shown to be more rapid at elevated temperatures [69].

It is unfortunate that the present state-of-the-art perfluorosulfonic acid polymer membranes like Nafion require liquid water for proton transport, limiting the operating temperature to about 85–95 °C. Composite membranes of Nafion with zirconium phosphate have shown enhanced performance at temperatures up to 130 °C. At higher temperatures various Nafion composites exhibit weakening chemical and physical stability. Besides, in order to sustain relative humidity above required 90%, the system has to be constructed to bear elevated pressures. [70]

Fortunately, there are also membrane candidates for high temperature polymer fuel cells, especially suitable for high levels of CO. Polybenzimidazole (PBI) membranes, doped with phosphoric acid for the proton conduction, maintain high ionic conductivity even at temperatures near 200 °C [71] and can tolerate CO levels of several percent [72,73]. Thanks to the higher temperature, electrode kinetics is faster and water management significantly easier [74]. With the enhanced CO tolerance, one could also give up using ruthenium, which tends to dissociate itself from platinum at high temperatures in acidic environments.

However, in the midst of the hype about high-temperature membranes, issues with lower power densities and weaker mechanical strength are sometimes dropped. Alternatives to Nafion usually require more platinum to provide equal performance, thus adding to the costs. Mechanical durability can be enhanced by using composite membranes [73] such as PBI-Nafion [75], but the development is still in process.

High temperatures seem to have potential in tackling many concerns with fuel cell operation. However, for mobile applications they are inconvenient. Chandan et al. [76] have recently reviewed the current status of high temperature fuel cells.

3 Experimental part

In the experimental part, the effects of carbon monoxide on cell performance and its mitigation were studied. The main objective of the experiments was to further develop air bleed methodology, using a special design of multisingle cell (MsC), segmented cells in series [77]. Anode exhaust gas was analysed to gain insight into the poisoning dynamics and the extent of carbon corrosion due to external air bleed.

All measurements were performed at VTT Technical Research Centre of Finland in Espoo between October 2012 and April 2013.

3.1 Experimental setup

In the MsC as segmented cells in series design, four single cells were stacked together. Typically the flow channels are arranged in parallel as in [78]. In the novel segmented-cell-in-series approach utilised here, anodes were connected in series, and only cathodes in parallel. This means that the anode outlet of the preceding cell was always the anode inlet of the following, which was executed by strategically blocking some of the internal gas distribution channels in the flow field plates. However, none of the air channels was blocked. The oxidant was supplied equally to the main entrance of each cell, allowing even distribution.

The current response of the MsC was measured with an in-house developed electrical arrangement. Each of the four cell segments, comprising the fuel cell, was connected to a DC load (LD 300, TTi, UK) controlled by a voltage signal from an external power supply (EX2020R, TTi, UK). By this arrangement, the segment currents could be examined, while operating all cells at the same potential. Similar approaches have also been reported elsewhere [79, 80].

Table 1 summarises operational parameters in the two experimental sets presented here. To make the cells gasproof, 350 µm thick polyolefin gaskets (Model 35 FC-PO100, Freudenberg, Germany) were installed between bipolar plates. These graphite plates (ISEM-3, Svenska Tanso, Sweden) were 88 mm long, 88 mm wide, and 20 mm thick, having single channel serpentine flow fields. The clamping pressure of the stack was adjusted by the number of disc springs (Belleville, UK) tightened on top of both end plates.

Table 1: Operational parameters in experiments.

Operational parameter	Exps. with Pt	Exps. with Pt−Ru
Temperature (K)	338	338 or 353
Relative humidity (%)	100	100
Cell area (cm^2)	25	25
MEA	Commercial	Commercial
GDL	Sigracet SGL 35 BC	Sigracet SGL 35 BC
MEA / GDL thicknesses (μm)	35 / 325	35 / 325
CO molar flow rate (mol s^{-1})	$7.3 \cdot 10^{-9}$	$7.3 \cdot 10^{-9}$
Catalyst loading (mg cm^{-2})	0.4 (anode) / 0.6	0.25 (both)

Figure 1 illustrates the experimental setup. Reactant flow rates, humidities, temperatures, and data logging were controlled using a test station (Arbin Instruments, USA). Gas humidification was realised by transporting reactants through heated bubblers inside the test station. The desired cell temperature was achieved by circulating deionized water through specific channels inside the bipolar plates. The temperature was verified by inserting a K type thermocouple in the middlemost segment of the stack. Temperature deviations between the cells were less than 1 K.

The cell was operated by feeding the cathode with compressed ambient air and anode with H_2. The air was cleansed of possible particle impurities by two filters (2000 series, Parker Hannifin Corporation, USA) before entering the cell. At the outlet, excess air was vented, before which moisture was condensed by a water trap.

The H_2 supplied was of high purity (in most experiments 99.999%). During the poisonings, H_2 entrained known trace levels of carbon monoxide. Before mixing, CO was in equilibrium with N_2 at a concentration of 901 ± 2 ppm. Check valves (C series, Swagelok®, USA) were installed in the H_2 and air bleed pipelines to prevent upstream contamination with CO. Inlet and outlet pressures of both electrodes were measured with pressure transducers (CTE7000 series, Sensor Technics, Germany).

Whenever air bleed was needed, synthetic air produced with a zero air gas generator (Model 76-818, Whatman™, UK) was introduced to the anode fuel stream. For both the air bleed and CO, an external control box (Series E-7000, Bronkhorst, The Netherlands) combined with mass flow controllers (EL-FLOW®, Bronkhorst, The Netherlands) was utilised. The latter were calibrated by a flow calibrator (Gilian®, Sensidyne, USA).
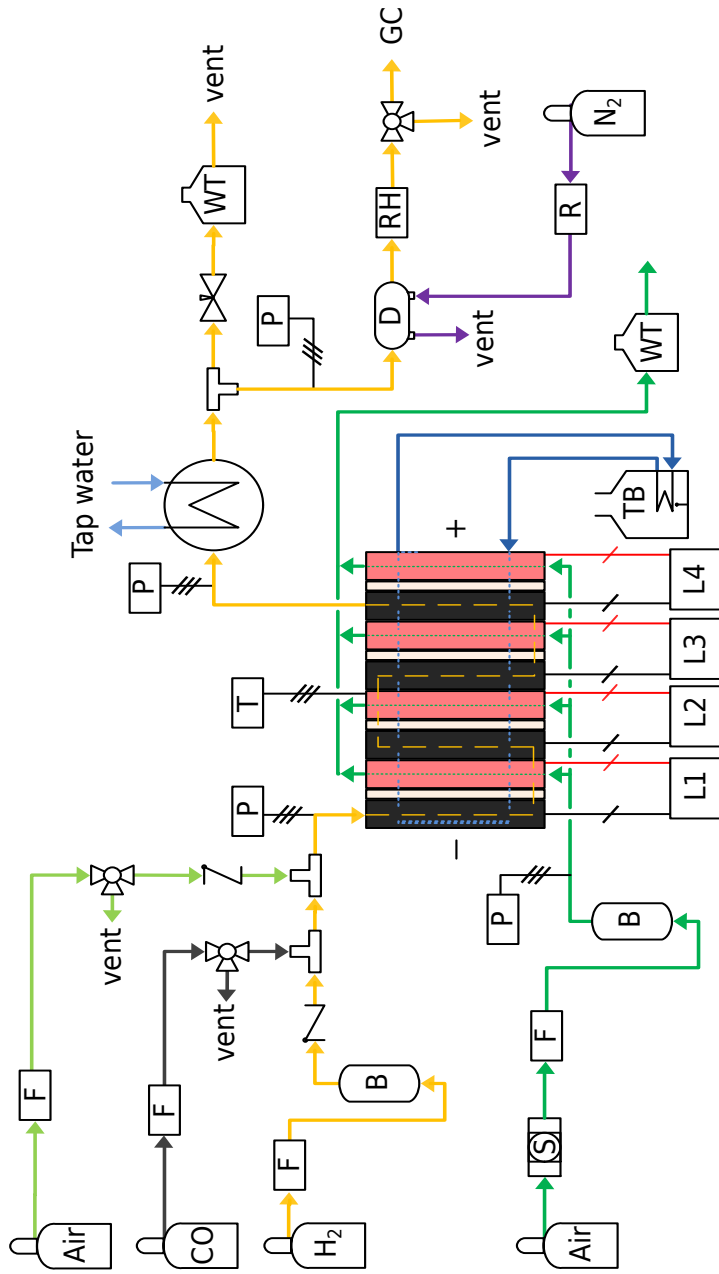
Figure 1: Scheme of the experimental setup. The MsC as segmented cell in series is in the middle. F = mass flow controller, B = bubbler (humidifier), P = pressure transducer, T = temperature transducer, H = heat exchanger, WT = water trap, D = dryer, RH = relative humidity probe, R = rotameter, GC = gas chromatograph, S = separators, L = load and TB = thermostatic bath.

Anode outlet gas composition was analysed with a gas chromatograph. For this purpose, the exhaust gas was dried in two stages, using a condenser and a membrane dryer. First, it was cooled in a coaxial pipe where tap water flowed in the opposite direction. Moisture was condensed by a water trap, after which the gas was further processed by passing it through a membrane module (FC$^{\text{TM}}$–Series, Perma Pure LLC, USA). A drying effect was accomplished by circulating N_2 at 353 K in counterflow at a flow rate of 1 dm^3 min^{-1}. The relative humidity of the dried exhaust gas was measured with a dew point and temperature probe (Humicap$^{\circledR}$, Vaisala, Finland) before entering the gas chromatograph.

3.2   Gas chromatograph

The composition of the anode exhaust gas was analysed with a gas chromatograph (6890 series, Agilent Technologies, USA), utilising a 1.83 m long packed column (Porapak Q, Agilent Technologies, USA) for the retention of gases and a flame ionisation detector (FID).

In FID, the analyte is burnt in H_2 flame to ionise it, resulting in a flux of charged species towards current collectors. The concentration of the species is directly proportional to the current measured. Since FID is not sensitive to CO or to CO_2 but it does ionise CH_4, the analyte was methanised after elution and before entering the ionisation chamber.

The GC was calibrated before every experiment, using a gas mixture of 10.2 ± 0.2 ppm CO and 9.63 ± 0.19 ppm CO_2 in equilibrium with He (Oy AGA Ab, Finland). During the experiments, a sample was programmed to be injected approximately every four minutes.

Because of the high overall number of GC samples, a Matlab routine was applied to facilitate the analyses. The code encompassed noise filtering and integration of CO and CO_2 peaks by trapezoidal algorithms.

3.3 Test procedures

Table 2 displays experimental differences between tests with pure Pt. In the first experiment, all cells were on purpose severely poisoned, which is why the MEAs were replaced by fresh ones for the rest of the experiments. The second was used as a reference test. In experiments 1.3, 1.4 and 1.5, the effect of anode stoichiometry was investigated, and the last three tests were designed to provide information about the carbon corrosion of fuel cell components.

The multisingle cell was operated potentiostatically throughout the experiments. Cell performance was left to stabilise at $I_{tot} \approx 60\,\text{A}$ at least for 45 min before injecting CO. Apart from the experiments 1.1 and 1.6–1.8 in Table 2, air bleed was introduced as soon as 20–25% of the total current or power was lost.

Air bleed was increased by steps of 0.2 percentage points, each level lasting 50 min. At the end of the last level, the cell was run with neat H_2 for 15 min. To ensure that the catalyst surface would be completely free of adsorbed CO residues at the beginning of the following experiment, regenerative air bleed of 1.8% was fed in for 15 min. Finally, the humidifiers were purged with nitrogen for 15 min.

Anode exhaust gas composition with respect to CO and CO_2 was analysed with a gas chromatograph throughout the measurements. Reproducibility of each experiment was verified by at least one repetition.

In the experiments 1.6–1.8, the objective was to trace the portion of CO_2 in the anode exhaust that resulted from the oxidation of carbon components, that is, MEA, GDL, and bipolar plate. Therefore, involvement of CO was eliminated from the experiment 1.6.

For dummy cell tests 1.7 and 1.8, the component configuration was partly modified. No current was drawn since the MEA was replaced by a polyimide film, and the cathode equivalent was equipped with GDL, whereas the anode not. Bipolar plates and gaskets remained in either compartment. Both gas distribution channels were assembled to be in series. Thus, just by rotating the MsC stack horizontally 180°, before proceeding to the experiment 1.8, it was possible to distinguish the CO_2 contribution of GDL from bipolar plate.

Table 2: Experimental test matrix for the MEA setup with Pt catalyst. In each experiment, cell temperature was 338 K, relative humidities of gases 100% and pressures 101.325 kPa. Molar flow rate of CO was kept constant at $7.27 \cdot 10^{-9}$ mol s^{-1}.

Exp.	$\dot{V}_{H_2}$ (cm^3 min^{-1})	$\dot{V}_{O_2}$ (cm^3 min^{-1})	λ_{H_2}	C_{CO} (ppm)	AB (%)
1.1	618.9	2489.2	1.48	16	2.0
1.2	635.5	2521.8	1.51	15	0.6 ... 1.6
1.3	508.4	2521.8	1.23	19	0.8 ... 1.4
1.4	635.5	2521.8	1.50	15	0.8 ... 1.4
1.5	762.6	2521.8	1.81	13	0.8 ... 1.4
1.6	635.5	2521.8	1.50	–	0.6 ... 2.0
1.7, 1.8	635.5	–	–	–	0.6 ... 2.0

Table 3: Experimental test matrix for the MEA setup with Pt−Ru catalyst. Relative humidities of gases were 100% and pressures 101.325 kPa. Molar flow rate of CO was kept constant at $7.27 \cdot 10^{-9}$ mol s^{-1}. The volumetric flow rate of O$_2$ was 2521.8 cm^3 min^{-1} throughout the tests.

Exp.	$\dot{V}_{H_2}$ (cm^3 min^{-1})	T (K)	C_{CO} (ppm)	AB (%)
2.1	635.5	338	16	2.0
2.2	635.5	338	15	0.1 ... 0.6
2.3	508.4	338	19	0.1 ... 0.6
2.4	762.6	338	15	0.1 ... 0.6
2.5	635.5	353	13	0.1 ... 0.6

When choosing the air bleed percentages, the focus was on finding the optimal level to stop the poisoning and also on representing the recovery in the most illustrative way. For this purpose, a literature survey was made to steer the course. A summary of this examination can be found in the paper published in parallel with this thesis [81].

One complementary mitigation method was applied by using state-of-the-art Pt−Ru MEAs. Table 3 summarises the details of this experimental set 2.

3.4 Calculations

To analyse the experimental data gained, it was necessary to know the molar flow rates of gases before and after the MsC. Whenever needed in calculations, standard conditions for temperature and pressure were applied as recommended by IUPAC. Molar flow rates of O_2 and H_2 fed to the cell were calculated using equation (9), assuming 100% coulombic conversion.

The corresponding volumetric flow rate of a reactant i was calculated by assuming ideal gas behaviour:

$$\dot{V}_i = \frac{\dot{n}_i RT}{P} \lambda_i \tag{24}$$

where R is the universal gas constant, T the temperature, P the pressure, and λ_i the stoichiometric coefficient defined in equation (9).

The CO concentration in poisonings, C_{CO}, was calculated on grounds of knowing the rate of the total flow entering the cell, $\dot{V}_{in}$, the flow rate of injected CO from the equilibrium mixture with N_2, $\dot{V}_{CO/N_2}$, and the CO concentration in that mixture, C_{CO/N_2}:

$$C_{CO} = \frac{\dot{V}_{CO/N_2}}{\dot{V}_{in}} C_{CO/N_2} \tag{25}$$

Air bleed percentages resulted from a comparison to the hydrogen flow rate:

$$AB\,(\%) = \frac{\dot{V}_{AB}}{\dot{V}_{H_2}} \cdot 100\% \tag{26}$$

Clearly, equation (26) does not give the exact percentage of air bleed since the flow rate of air is omitted from the supposed total flow in the nominator. However, this approximation is convenient and produces negligible error within the applied flow ranges.

3.5 Sources of CO_2

One central part of the analysis of the results presented in the next section was the amount of CO_2 at the anode outlet. Owing to the complexity of the experimental setup, all CO_2 detected with the GC was not resulting from the electrode reactions of interest. Therefore, all possible sources of CO_2 were carefully identified as follows. Table 4 summarises the possible error sources of CO_2 and suggestions to overcome the problems.

i) CO_2 from oxidation of CO by air bleed

   In the ideal case, this is the only source of CO_2. Without other sources it would be straightforward to examine the rate of CO electrooxidation, which would be in direct relationship with the CO_2 detected at the cell outlet.

ii) CO_2 from oxidation of carbon components

   In principle, all carbon parts of the fuel cell are prone to oxidation, although this is most probably a slow process as discussed in Section 2.5.1. In addition to the preceding source of CO_2, this was the only one that was not subtracted away in the CO_2 molar flow analysis of the experimental data. On the contrary, the following sources of error were taken into account and their contribution was made as negligible as possible.

iii) CO_2 impurities in H_2 fuel

   All tests were performed using high quality H_2 (at least 99.999% pure) except experiment 1.1. In that case, the cell was fed with lower quality H_2 ($C_{CO_2} < 20$ ppm). Before every poisoning, the fuel cell operation was allowed to stabilise for at least 45 minutes so that if fuel impurities had caused some errors, they would have been systematic and taken effortlessly into account in the analysis.

iv) CO_2 in air bleed

   Locally produced synthetic air was utilised as the source of oxygen for air bleeding. Its composition was analysed with GC to contain traces of CO_2 (75.9% N_2, 22.96% O_2, 0.94% Ar, 0.0230% CO_2, and 0.177% undefined impurities), which probably caused minor errors in CO_2

Table 4: Error sources of CO_2 and their elimination.

Error source of CO_2	Solution
Carbon corrosion	Dummy cell experiment
Fuel impurities	Use high quality H_2 and verify the purity
Air bleed impurities	Use synthetic air or pure O_2 and verify the purity
Membrane crossover	Feed the cathode with synthetic air
CO_2 in humidifier	Pre-boiling

molar flow rates measured at the highest air bleed levels. To eliminate this, it is recommended to use bottled synthetic air (80% N_2 and 20% O_2).

v) CO_2 diffusing from the cathode

Because the cathode was fed with air, there was a CO_2 concentration gradient towards the anode. This resulted in a constant baseline of CO_2 throughout the measurements. During cell stabilisation periods, the crossover rate of CO_2 was estimated with GC to be $2.5 \cdot 10^{-9}$ mol s^{-1} which is in good agreement with $1.6 \cdot 10^{-9}$ mol s^{-1} reported in [82].

vi) CO_2 dissolved in the humidifier water

The humidifiers were filled with deionised water at the beginning of every experiment. This was realised to account for one additional source of CO_2, especially when temperature was increased. The dissolved CO_2 was liberated by heating the humidifier and feeding H_2 through it. To tackle this source of error, the CO_2 level at the anode outlet was always allowed to stabilise, before moving on to the poisoning.

4 Results and discussion

4.1 Pt catalyst

4.1.1 Cell response to CO poisoning and air bleed

Figure 2 shows an exemplary current response of the MsC as segmented cell in series under CO poisoning. The vertical axis displays relative decreases from the original values of respective cell currents. All segments followed the same pattern: Once CO entered the inlet of the cell, current started to decrease gently. This was followed by a steeper drop, finally levelling off and resulting in marginal current of about 3 A, corresponding to about 18% of the original segment current. In this experiment 1.1, lower quality hydrogen (impurity levels: O_2, H_2O and $CO_2 < 20$ ppm each, $N_2 < 500$ ppm) was used.
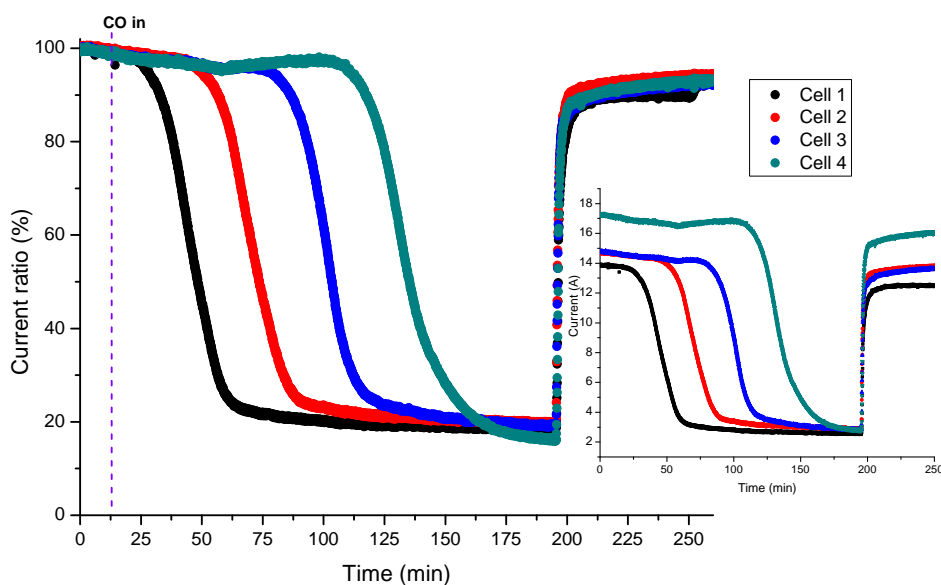

Figure 2: Current response of experiment 1.1. Total current was originally 60 A and cell voltages constant at 600 mV.

28

Filter analogy

Figure 2 shows that the cell response to the presence of CO was immediate. It is noteworthy that the segments seemed to become poisoned almost one by one but not quite. For example, at $t = 50$ min, the current of cell 2 was already declining, even though the catalyst sites of cell 1 were apparently not totally covered by CO. The same pattern was repeated with the remaining segments.

The phenomenon can be illustrated by analogy with filters: as soon as the preceding Pt filter is no longer able to hold all flowing CO, some of this will break through to the next filter. Breakthroughs can be attributed to increasing repulsions near the CO-free sites due to hydrogen being replaced by more massive CO molecules in the neighbouring sites. Analysis of this phenomenon is essential for considerations of recirculating the unused fuel [77], thus improving the system efficiency.

Greater repulsions alone may not, however, explain why the cells do not completely lose their ability to function. It is suggested in literature that the CO coverage on Pt approaches one even at low concentrations [35]. In experiment 1.1, however, this does not seem to be the case as can be inferred from the marginal current between $t = 175 \ldots 195$ min. This may be, for example, because of internal air bleed and mass transfer problems encountered by CO.

Effect of air bleed

Figure 3 represents the molar flows of CO and CO_2 at the anode outlet. In accordance with the filter analogy, the CO level at the outlet started to deviate from zero at around t = 100 min when the current of cell 4 had just begun to fall. At $t = 200$ min, the oxidative role of air bleed is clearly demonstrated by the simultaneous decrease in CO and increase in CO_2 molar flow rates. As a result, the cell performance was remarkably improved after $t = 195$ min in Figure 2.

At its highest, the molar flow rate of CO attained $4.2 \cdot 10^{-9}$ mol s^{-1} being $3.1 \cdot 10^{-9}$ mol s^{-1} less than what was fed in. This implies that the CO adsorption rate was still on the increase until the air bleed was launched, which is supported by the slight but continuous decrease in current after $t = 175$ min. After injecting oxygen to the anode, sudden increases both in
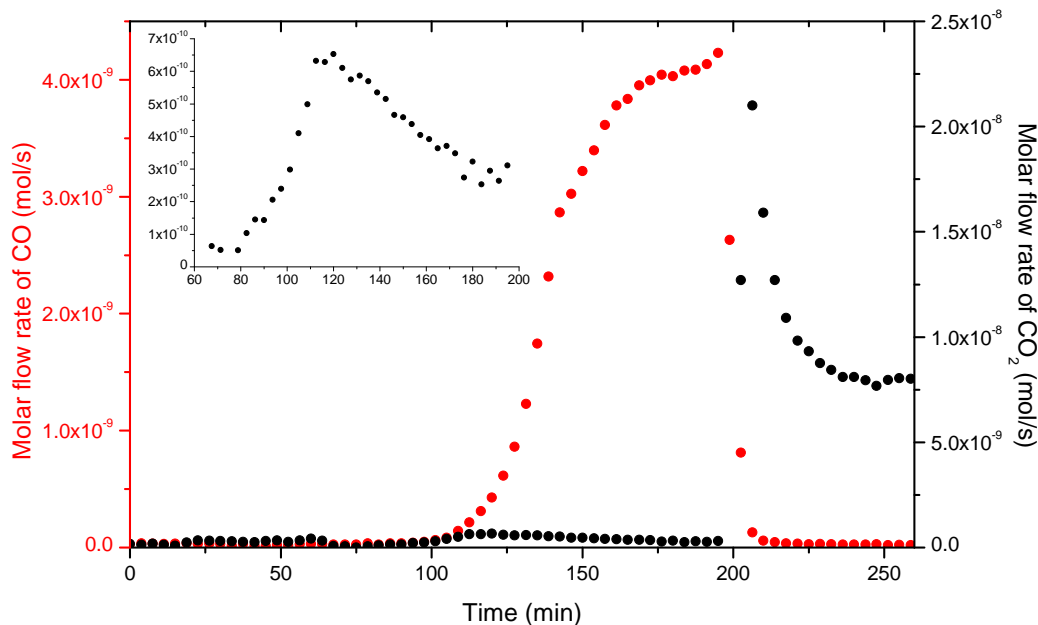
Figure 3: Molar flow rates of CO and CO_2 at the anode outlet in experiment 1.1.

current and CO_2 level were observed at the outlet as verified by Figures 2 and 3. Due to the simultaneousness, the intense CO_2 peak at $t = 206$ min can be deduced to originate from the electrooxidation of previously accumulated CO covering Pt sites.

It is noteworthy that 2% air bleed was after all enough to recover 93% of the cell performance but not more. This could not be explained away by some ongoing process. Namely, after the currents had reached plateaus, implying equal adsorption and desorption rates of CO, there was no CO coming out of the anode according to Figure 3. Besides, the molar flow rate of CO_2 at the outlet eventually attained the amount of CO fed in, so the incomplete recovery was most likely not because of too little air bleed. Consequently, possibly two explanations remain: either CO left the cells with a very slowly recoverable state or then also the cathode suffered from impurities, which is here left at the level of speculation.

30

Mass balance of CO

The mass balance of CO was closely examined in a research [81] conducted in parallel with this thesis. By integrating the molar flow rates of CO and CO_2 as a function of time, the molar amount of CO adsorbed on the overall catalyst area could be obtained. This result was obtained by subtracting the molar flow rates of CO breaking through and CO_2 from the total amount of CO fed in.

For this subtraction, three integral areas were distinguished in Figure 3: The first, relating to the total amount of CO fed in, was rectangular having the constant height of $7.3 \cdot 10^{-9}$ mol s^{-1} of CO and the width of the period between opening and closing the CO valve. The second was the area under the gradual increase in CO, indicating the amount of CO breaking through. The third was the area under the peak resulting from the introduction of air bleed, corresponding to the proportion of CO being oxidised to CO_2.

According to the calculations, the molar amount of CO adsorbed was $5.4 \cdot 10^{-9}$ mol s^{-1} in experiment 1.1. This means that as much as 85% of all CO remained on the catalyst surfaces. Even so, as stated previously, 93% of the original performance was restored. This implies an interesting result: a considerably smaller amount of free catalytic sites was enough to generate almost the same current as before any introduction of CO.

4.1.2 Air bleed optimisation

In order to find the optimal air bleed level, CO was oxidised by stepwise addition of oxygen to the fuel stream. Figure 4 represents the resulting current response. In the current scale, cell 1 was lower in performance than the others due to the previous unfortunate operation with somewhat dry hydrogen. The effect of air bleed was nevertheless evident. CO entered the first cell at $t = 15$ min and therefore the currents of the first and the second cell started to decrease steeply. As soon as the first air bleed step was introduced, the current of the first cell was slightly recovered and the poisoning of the second became more gentle.

Air bleed of 0.6% clearly helped, but it was not enough to consume all the CO entering the cell. The next step seemed to be the closest approximation
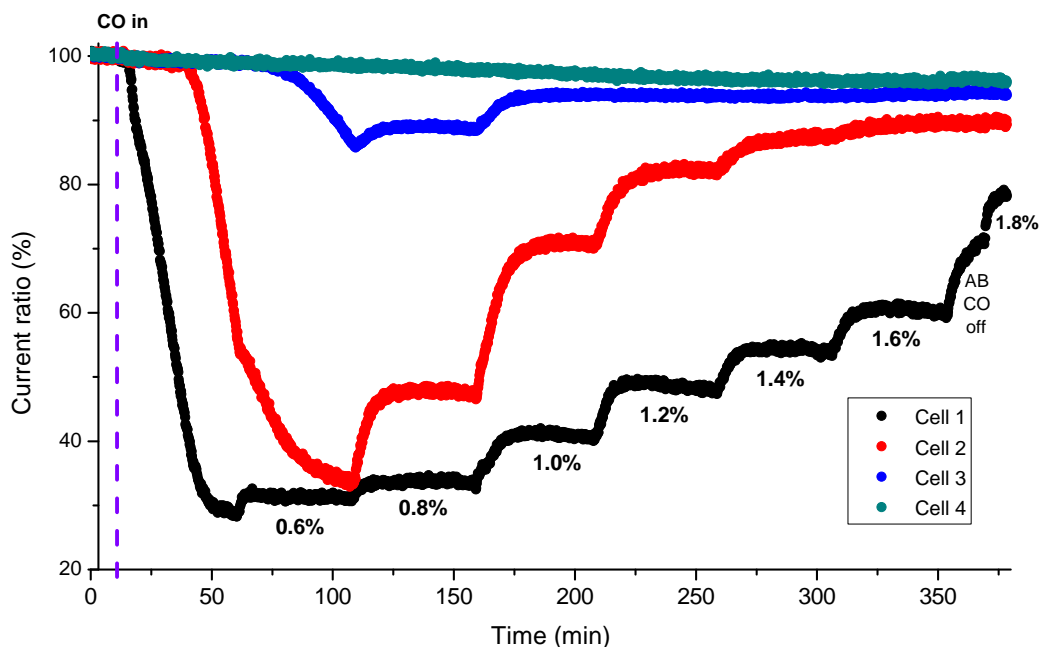
Figure 4: Current response of experiment 1.2. Cell voltages were constant at 670 mV. Air bleed percentages are marked in the figure.

of the optimal level. The currents reached a steady state, indicating equal adsorption and desorption rates of CO.

Again, since no CO was detected at the anode outlet, all CO fed in must have been electrooxidised to CO_2. This is also supported by the CO_2 molar flow rate at the anode outlet in Figure 5. During the second air bleed step, starting at around $t = 110$ min, CO_2 molar flow rate at the outlet reached that of CO at the inlet. This flow rate and the currents staying constant until the next air bleed step implied that there was no more free CO within the cell segments.

As the air bleed percentage was increased, the performance of all cell segments was improved, especially that of the second and the third. The first cell recovered in a consistent manner but notably less than the rest, which was a common observation throughout the experiments. Even when the CO valve was closed and 1.8% air bleed was injected for regenerative purposes, no more than 80% of the original performance was recovered. This might result, for instance, from repeated total poisonings of the first cell or
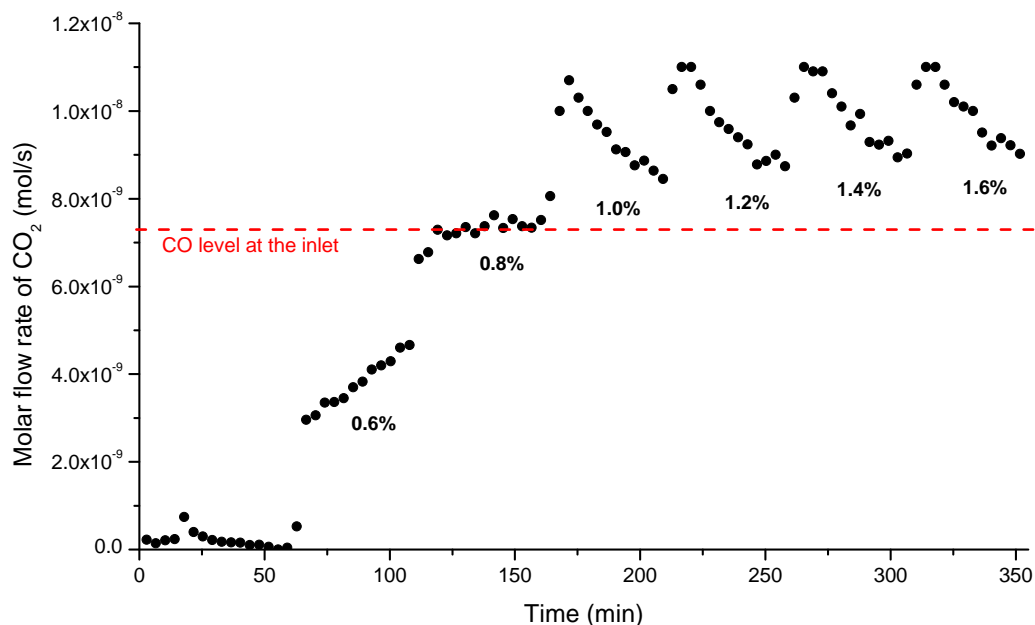
Figure 5: Molar flow rate of CO_2 at the anode outlet in experiment 1.2. No CO detected in the exhaust gas.

some undefined impurities entrained by water only to the first inlet, thus leaving the other cells undisturbed.

Carbon corrosion

It is evident that the higher the air bleed, the greater portion of the already adsorbed CO was electrooxidised away from all platinum surfaces. In Figure 5, this behaviour is associated with the CO_2 peaks appearing at around $t = 170$ min, $t = 220$ min, $t = 270$ min, and $t = 320$ min. Between these time intervals CO_2 molar flow tended to a steady state.

Interestingly, 0.8% air bleed appeared to be enough to consume all CO entering the cell. Higher air bleed levels seemed to attain a higher steady state than the $7.3 \cdot 10^{-9}$ mol s^{-1} of CO fed in, indicating that also something else besides CO was being oxidised to CO_2. Since the last four error sources of CO_2 of the list in Section 3.5 have been eliminated during the

33

analysis, the steady state could mainly result from two sources: continuous oxidation of CO entering the cell and the plausible corrosion of carbon components.

The final steady state lies close to $9.0 \cdot 10^{-9}$ mol s^{-1}. After subtracting the constant CO flow from this value, $1.7 \cdot 10^{-9}$ mol s^{-1} remains. Carbon corrosion might account for the surplus. It also seems possible that the corrosion becomes more intense with increasing air bleed since the CO_2 steady state resulting from 0.8% air bleed is lower than the one resulting from 1.6%. Similar results were also obtained in dummy cell experiments.

The corrosion of carbon components was desired to be kept at minimum and the recovery of the cells as high as possible. Therefore, on the basis of the preceding examination, it was decided for the following poisonings of the experimental set 1 to keep the lower air bleed limit to 0.8% and the upper to 1.4%.

4.1.3 Effect of anode flow rate

Figure 6 displays the current response of the MsC as segmented cell in series with respect to three different anode flow rates. For the sake of clarity, the fourth cell was omitted as the poisoning did not proceed that far. Since especially the performance of the first cell was continually deteriorated during the course of the experiments, the currents were again expressed as ratios to facilitate comparison.

The molar flow rate of CO at the anode inlet was kept the same as before. Therefore, as Table 2 indicates, while anode flow rate was increased, CO concentration fell accordingly. Slightly higher CO concentration led to more severe poisoning, which was verified by a greater drop in the current of the first cell in experiment 1.2 (lowest H_2 flow rate) than in experiment 1.4 (highest H_2 flow rate).

Changes in H_2 flow rate affected also cell recovery by air bleed. Oxygen concentration was kept the same in each experiment during corresponding air bleed steps. This means that the molar flow rate of oxygen at the inlet was increased in accordance with the anode flow rate, which mimics an open anode system in industrial stationary PEFC applications.

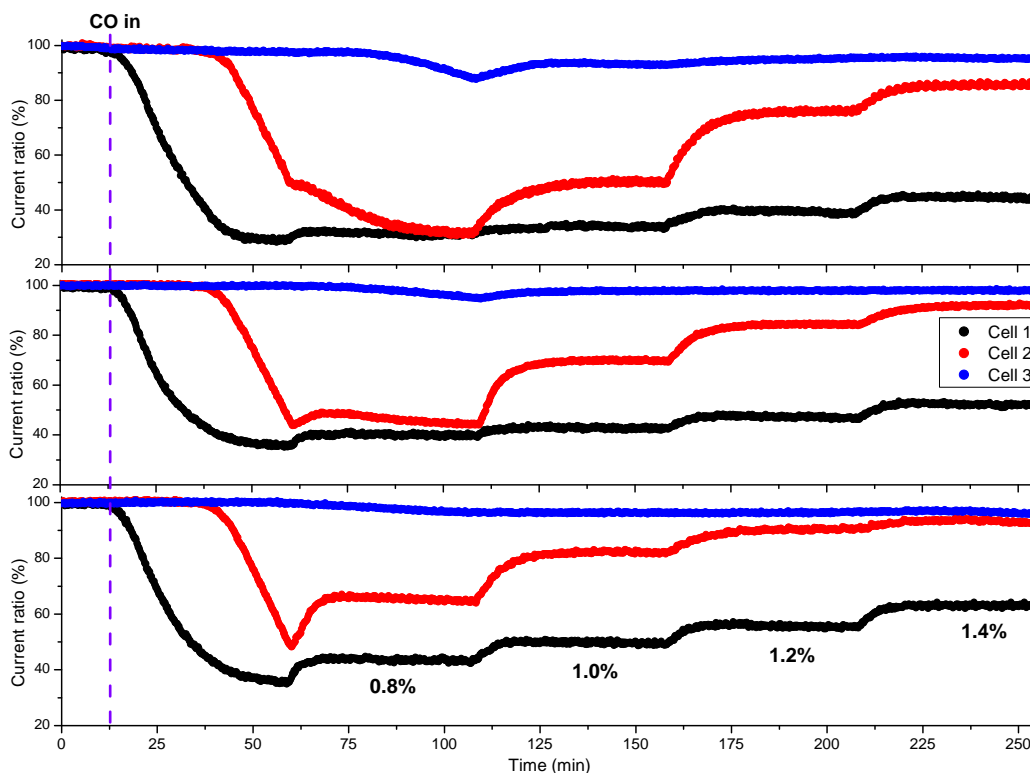With the increase in molar flow of oxygen in mind, it is clear why the 1.4%

34

Figure 6: Current responses of experiments 1.3 (uppermost), 1.4, and 1.5. Cell voltages were constant at 660 mV, 650 mV and 660 mV, respectively.

air bleed recovery of the first segment remained below 60% when having the low and intermediate H_2 flow rates but not when having the highest one. For the very same reason, 0.8% air bleed was enough to stop the poisoning only in the latter case. From the more intense poisoning of the second and the third cell in Figure 6, it can be inferred, that less CO was able to break through the second cell with the intermediate than with the low stoichiometry.

The incomplete recovery with 0.8% air bleed gains further support from the CO_2 molar flow rates at the anode outlet in Figure 7. No CO was detected at the outlet in any of the three experiments, so the $7.3 \cdot 10^{-9}$ mol s^{-1} of CO fed to the cell was always either oxidised to CO_2 or adsorbed onto the catalyst, or both were the currents not in steady state.
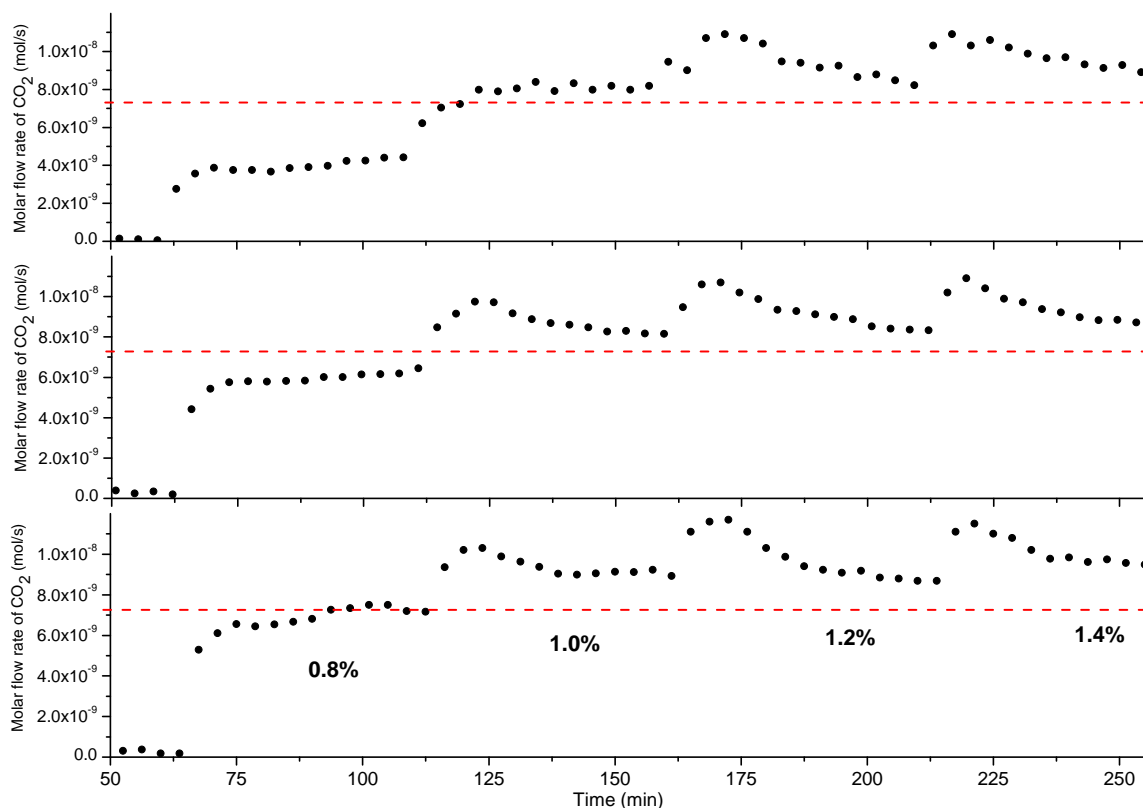
Figure 7: Molar flow rates of CO_2 at the anode outlet in experiments 1.3 (uppermost), 1.4, and 1.5.

The latter was the case with the first air bleed step in experiments with the low and intermediate flow rates as can be deduced from the average values for CO_2 flow rate at the outlet, $4.5 \cdot 10^{-9}$ mol s^{-1} and $6.8 \cdot 10^{-9}$ mol s^{-1}, respectively. For 0.8% air bleed, the minimum threshold for CO_2 in anode exhaust gas indicating the oxidation of $7.3 \cdot 10^{-9}$ mol s^{-1} of CO was exceeded only with the highest H_2 flow rate. Together with this information and the plateau seen in current response in experiment 4, it was evident that the poisoning had been stopped by 0.8% air bleed.

What highlights the intricate role of anode flow rate in the poisoning, is the difference in recovery between 1.0% and 0.8% air bleeds with the low and intermediate H_2 stoichiometries, respectively. The molar flow rates of O_2 are equal, yet in the former case the poisoning is stopped but in the latter it is not. This proves that the volumetric flow rate of H_2 should not be neglected on closer inspections of the CO poisoning taking place in channels with serpentine flow field geometry.

36

Table 5: Comparisons of the anode flow rate with the state of poisoning.

Exp.	$\dot{V}_{H_2}$ (cm^3 min^{-1})	AB (%)	C_{CO} (ppm)	$\dot{n}_{O_2}/\dot{n}_{CO}$	Poisoning
3	508.4	0.8	19	94	Continuing
		1.0		117	Stopped
4	635.5	0.8	15	117	Continuing
		1.0		147	Stopped
5	762.6	0.8	13	141	Stopped
		1.0		176	Stopped

As an experimental result, this observation is unique. Modelling studies have yielded suggestions that this flow rate effect could be traced to two overlapping explanations: the residence time of the fuel mixture in the flow channels [83] and the H_2 partial pressure drop towards the end of the channels [84]. Lower anode flow rate, that is longer residence, provides O_2 with more time to diffuse away from the flow channel through the GDL, thus leading to increasing interaction with the poisoning agent. Furthermore, with only low excess of H_2 at the inlet, the fraction of O_2 in the fuel is notably increased towards the end of the channel. In this way, air bleed effect might be enhanced.

Of course, the same should hold true for CO. However, because the amount of O_2 greatly outnumbers that of CO, longer residence time and H_2 depletion may play a more pronounced role in the function of air bleed. The anode flow rate effect is summarised in Table 5. Molar flow rates of O_2 entrained by synthetic air were calculated straightforwardly from equations (26), (24), and (9). The table shows that irrespective of the equal molar ratios of O_2 and CO in experiments 1.3 and 1.4, air bleed was more effective in the first case. It seems there cannot be any other explanation than the differing anode flow rate.

4.2 Pt−Ru catalyst

4.2.1 Cell response to CO poisoning and air bleed

Figure 8 shows a complete CO poisoning of the MsC as segmented cells in series with Pt−Ru MEAs. The mitigative effect of adding ruthenium was

obvious: each segment current decreased by only 2 A, whereas with pure Pt the fall was more than 10 A as depicted in Section 4.1.1. In percent scale, currents dropped to about 85% and 18%, respectively.

The shapes of the current curves were also rather dissimilar. When Pt−Ru catalyst was under poisoning, the asymptotic fall towards the final current was clearly more gentle and slower, and even the steep portions of the poisoning gradients were notably smaller.
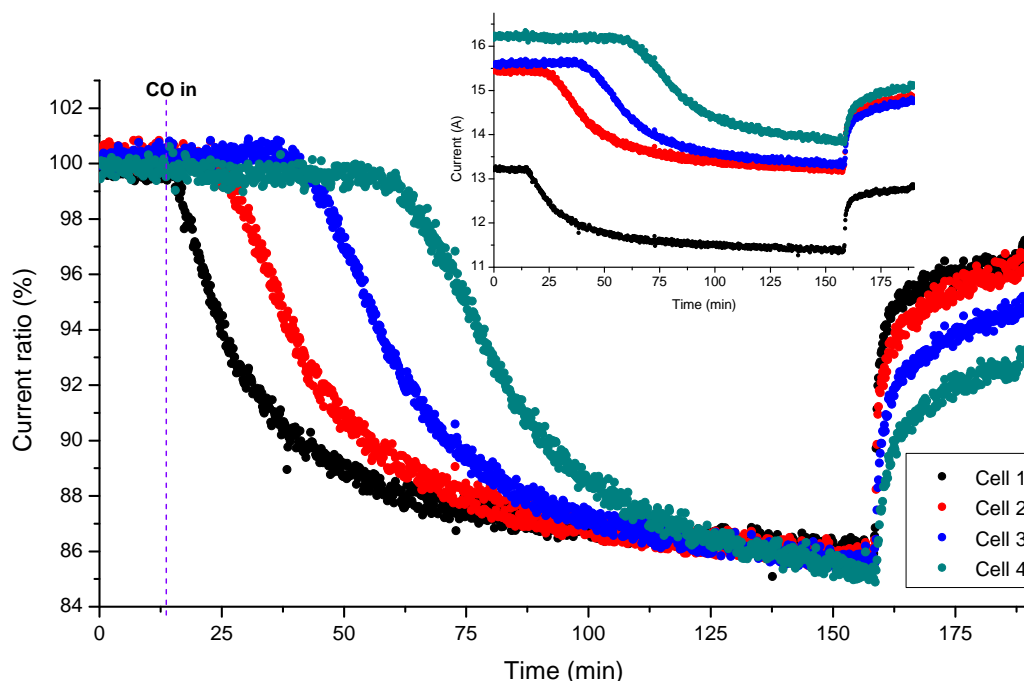

Figure 8: Current response of experiment 2.1 with Pt−Ru catalyst. Cell voltages were constant at 680 mV.

Another difference was more pronounced breakthrough of the poisoning agent. After the current of the preceding segment had begun to decrease, it took only approximately 10 minutes for the next cell to get exposed to CO. This trend is also supported by Figure 9, according to which it took about 70 min for the molar flow rate of CO to reach steady state of about $3.8 \cdot 10^{-9}$ mol s^{-1} at the anode outlet. With Pt catalyst, the corresponding duration was at least 100 min, as is clear from Figure 3.

The above-mentioned indications of greater CO tolerance of the Pt−Ru catalyst result at least from the lower onset potential for CO electrooxida-
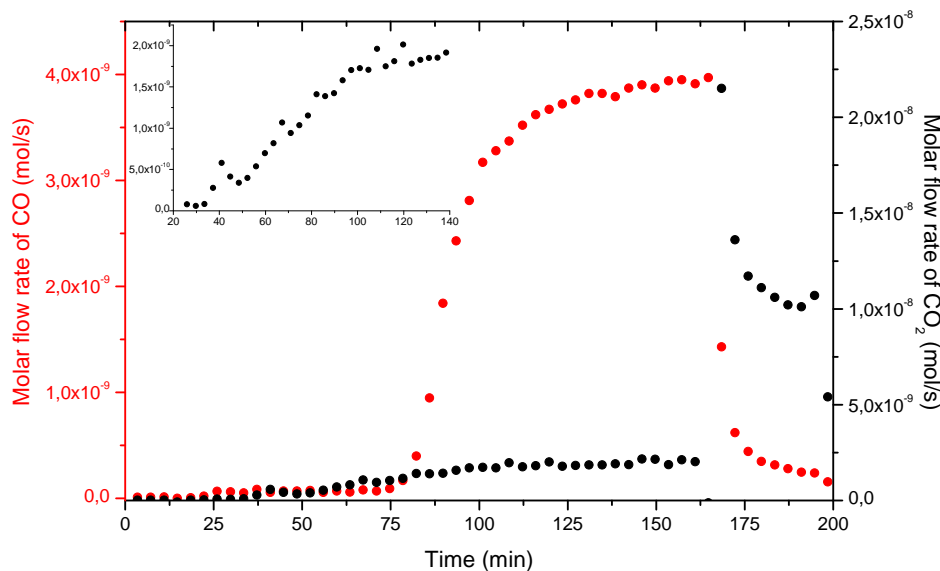
38

Figure 9: Molar flow rates of CO and CO_2 at the anode outlet in experiment 2.1.

tion [85] and, thus, more facile removal of the poisoning agent. The continuous oxidation was verified by the steady increment in CO_2 detected at the anode outlet, starting shortly after CO was introduced to the first cell, as illustrated in Figure 9. The further the poisoning proceeded, the more active area there opened for the electrooxidation, and therefore, the more CO_2 was measured with the GC. Oxygen for the electrooxidation was most probably provided by internal air bleed or water in the fuel.

A little before starting the air bleed, approximately $2.5 \cdot 10^{-9}$ mol s^{-1} of CO_2 was coming out of the MsC. When added to the amount of CO reaching the anode outlet at the time, this makes a total of $6.3 \cdot 10^{-9}$ mol s^{-1}, suggesting that some of the CO fed in was still adsorbing onto the catalyst. This observation is in good agreement with the slight but continuous decrease of all cell currents.

Once 2% air bleed was initiated at around $t = 165$ min, CO molar flow rate dropped close to zero. In turn, the molar flow rate of CO_2 rose to a value implying complete oxidation of CO fed in. The increase went through a sharp peak caused by electrooxidation of accumulated CO on the electrode. In this way, air bleed restored 95% of the overall current.
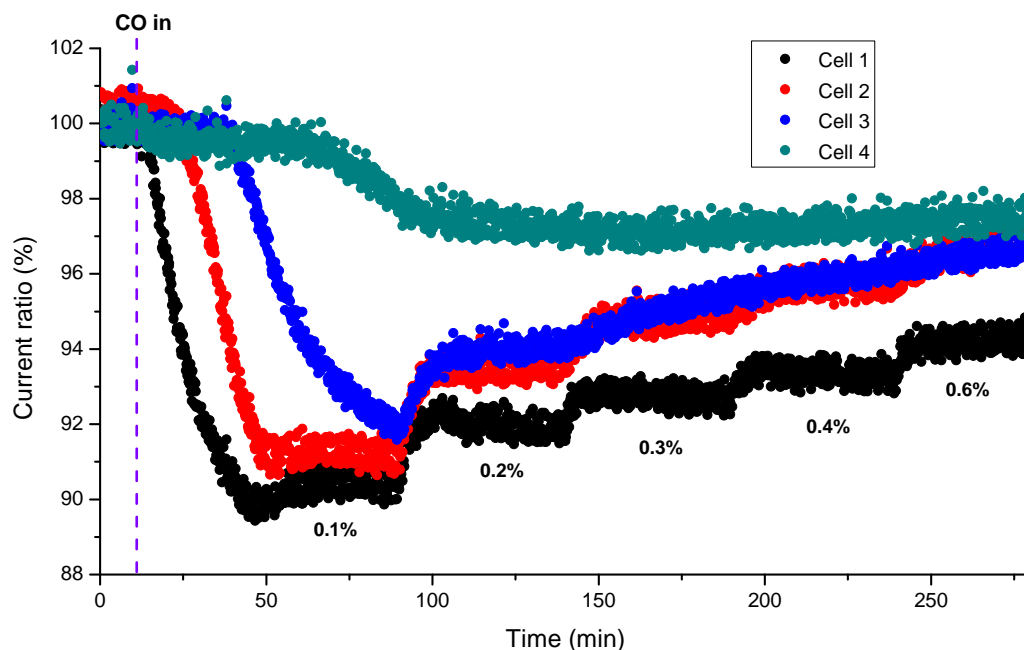
Figure 10: Current response in experiment 2.2 with Pt−Ru catalyst. Cell voltages were constant at 680 mV.

4.2.2 Air bleed optimisation

Figure 10 illustrates a similar air bleed step experiment to what was described in Section 4.1.2 with pure Pt catalyst. Air bleed percentages were notably reduced since the addition of Ru to the catalyst was known to have a beneficial effect on the electrooxidation of CO. Indeed, according to the current response in Figure 10, already 0.2% air bleed was enough to stop the severe poisoning, which was a fifth of the oxygen needed with pure Pt. Elsewhere, half the amount needed for Pt has been observed to be sufficient for equal recovery of Pt−Ru [86].

On closer inspection of the current of cell 1, Figure 10 reveals that a slight poisoning continues until the last air bleed step. This is further supported by Figure 11 in which the molar flow rate of CO_2 reaches the value of CO fed in only with 0.6% air bleed.

It also seems that the electrooxidation of the accumulated CO was more rapid than with Pt because the CO_2 peaks at around $t = 78 \, \text{min}$, $t = 125 \, \text{min}$,
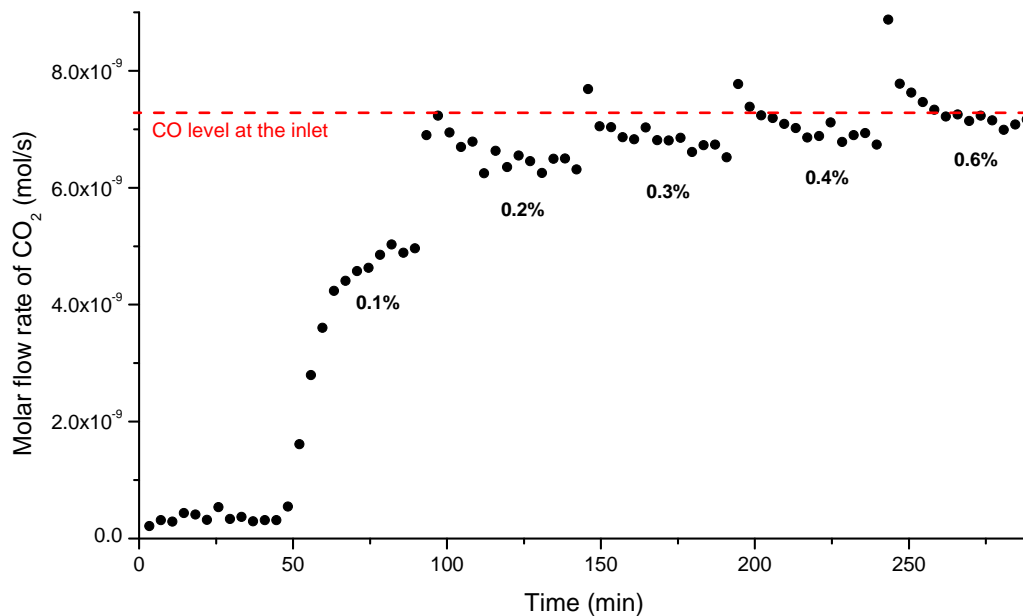
40

Figure 11: Molar flow rate of CO_2 at the anode outlet in experiment 2.2.

$t = 175$ min, and $t = 225$ min were sharper. This might be a consequence of the lower onset potential for CO electrooxidation, giving rise to a greater overpotential and thus a faster reaction.

Appendix A represents figures concerning the current responses and respective molar flow rates of CO_2, when having Pt−Ru catalysts with low and high anode stoichiometries. The characteristic features of the poisoning with the intermediate flow rate analysed above are also visible with these two other stoichiometries. Furthermore, similar analysis as given in Section 4.1.3 can be easily applied to Pt−Ru case as well.

4.2.3   Elevated temperature

Once the cell temperature was raised by 15 K, the efficiency of the air bleed was lowered. Figures 12 and 13 represent this interesting result: the selectivity of air bleed for oxidising CO appears lower at $T = 353$ K than what it was at $T = 338$ K according to Figure 11. The most apparent indication of this was CO breaking through the last cell starting from $t = 75$ min at the higher temperature. With 0.1% air bleed, further support for the inhibited electrooxidation of CO was provided by molar flow rates of CO_2 that were $2.9 \cdot 10^{-9}$ mol s^{-1} and $4.9 \cdot 10^{-9}$ mol s^{-1} for $T = 353$ K and $T = 338$ K, respectively. Only the last air bleed step of 0.6% could decrease the molar flow rate of CO close to zero at the outlet.
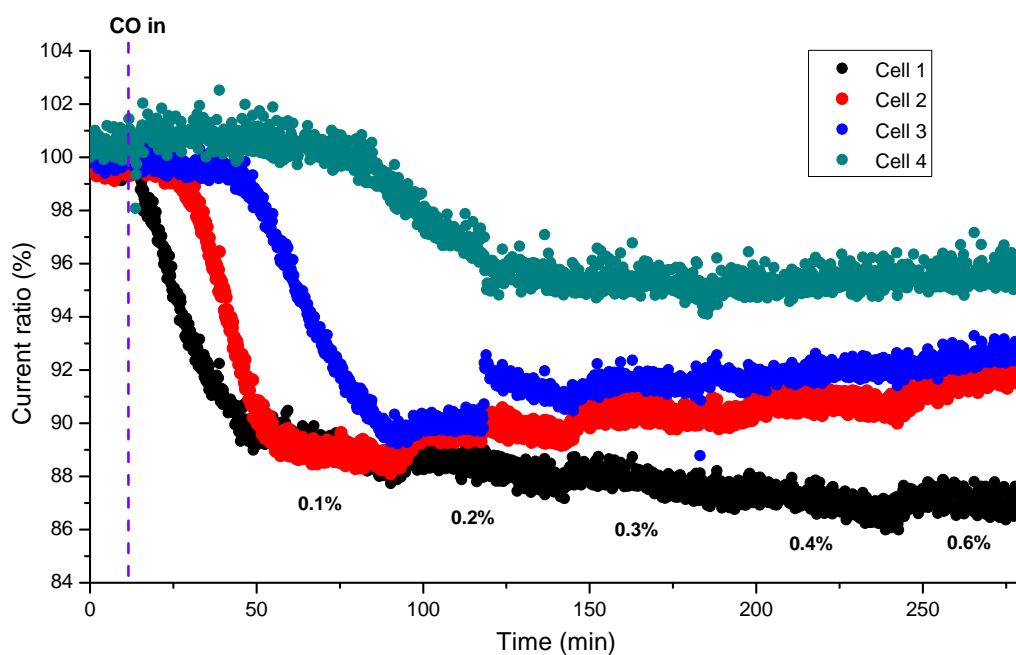

Figure 12: Current response of experiment 2.5. Cell voltages were constant at 630 mV.

The consequences of the diminished mitigation of CO poisoning can be seen in the current response in Figure 12. The current of cell 1 was practically on constant decrease and the recovery of the other cells also appeared somewhat damped in comparison with the lower temperature case. Approximately 93% and 97% of the total current were restored at $T = 353$ K
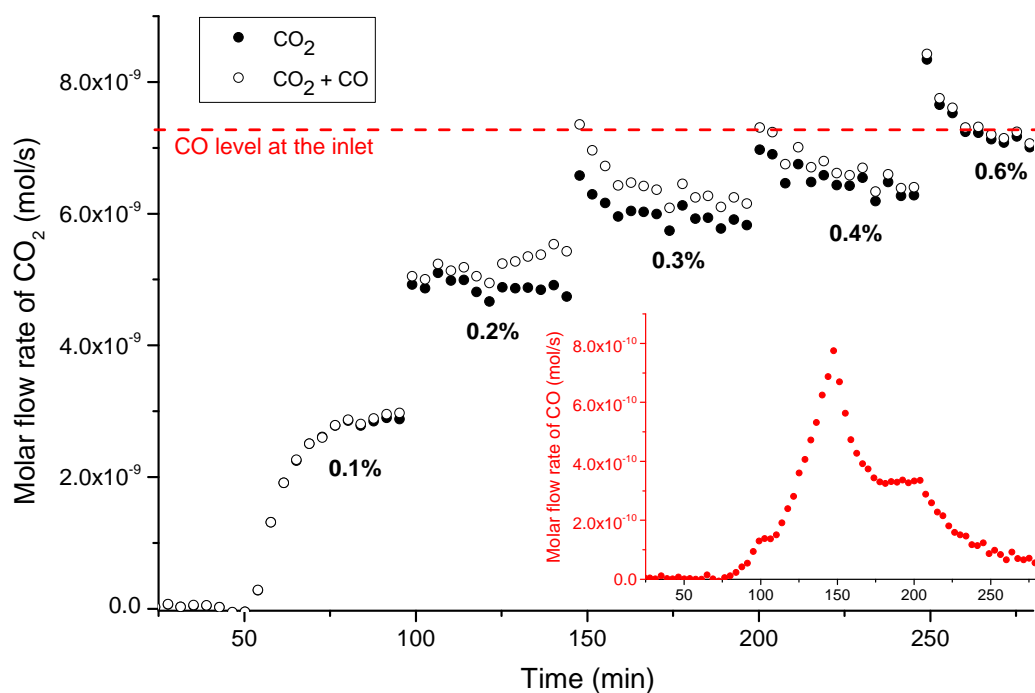
Figure 13: Molar flow rates of CO_2 and CO at the anode outlet in experiment 2.5.

and $T = 338$ K, respectively. In Figure 13, the hindered electrooxidation at higher temperature is also in accordance with smaller or non-existent CO_2 peaks previously associated with the liberation of Pt sites from accumulated CO.

These observations suggest a novel approach to the combination of different mitigation methods. For the state-of-the-art MEAs that can be operated at elevated temperature, it seems favorable to lower the temperature, before introducing air bleed to electrooxidise CO. After the current has been restored to the desired level, the cell temperature can be raised back to the original value.

43

5 Conclusions

In this work, a new methodology was employed for combining different techniques to mitigate the CO poisoning of a PEMFC. The poisoning dynamics was examined with the help of a unique arrangement of MsC as segmented cell in series. Conclusions were based on the current response of potentiostatically operated stacks and a careful molar flow rate analysis of anode exhaust gas composition.

The methodology was successfully tested with a Pt catalyst at 338 K and with a state-of-the-art Pt−Ru catalyst also at 353 K. Appropriate air bleed levels between 0.1% and 2.0% were applied with three different H_2 flow rates and CO concentrations. The focus of the analysis was on the poisoning dynamics and determining the optimal air bleed level for stopping the poisoning and recovering the cell performance.

By analysing the mass balance of CO during the poisoning, it was demonstrated that only a small fraction of the electrochemically active area may be enough to produce almost full current. Once more of the remaining free catalyst sites are blocked by CO, the performance begins to degrade. Due to increasing repulsions near free Pt sites, some of the CO will gradually start preferring to break through to the next cell, eventually leaving the CO coverage of the preceding cell below one.

It was also discovered that by lowering the volumetric flow rate of H_2, thus increasing the residence time of CO in the flow channels, one may intensify the severity of the poisoning. However, when air bleed is applied, its effectiveness should be enhanced as well. For the Pt catalyst and all three H_2 flow rates investigated here, it was found that to stop the poisoning, an O_2/CO molar ratio of at least 117 was required at the anode inlet, being in the range of 0.8% to 1.0% air bleed with respect to total volumetric flow rates.

Pt−Ru was observed to exhibit a notably higher CO tolerance than Pt. As a result of total poisonings, only 15% of the overall current was lost with Pt−Ru, while with Pt the loss was 82%. This greater tolerance with Pt−Ru was traced to lower onset potential for the CO electrooxidation, which was supported by faster formation of CO_2 with air bleed on and even without. Namely, a steady increase in the molar amount of CO_2 was observed during the course of CO adsorption at the anode outlet. Once 2% air bleed was launched, 95% and 92% of the original overall performance

was restored with Pt−Ru and Pt, respectively. In order to just stop the poisoning, only about a fifth of the oxygen required with Pt was needed with Pt−Ru.

The effectiveness of air bleed was observed to be lower at elevated temperature with Pt−Ru. Apparently, the selectivity of oxygen to oxidise CO was lower at 353 K than at 338 K. Therefore, a novel approach was suggested concerning the combination of air bleed and higher temperature operation of a PEMFC: after some performance degradation caused by CO, the cell temperature should be lowered for the duration of the air bleed to attain optimal recovery.

For further optimisation of the air bleed and understanding of poisoning dynamics, it would be interesting to gain insight into the mass balance of CO after each cell segment. This would provide more precise information about the effect poisoning has on the local efficiency of the catalyst, which might also help in explaining the cumulative performance loss of the first cell after consecutive poisonings.

By examining the amounts of CO remaining adsorbed to a segment, one could approach conclusions on the fraction of electrochemically active area needed for a certain level of performance. Detailed information about the spatial distribution of CO may help to track the CO coverage as a function of time during the poisonings. This would be valuable because the coverage does not affect only the cell performance but also the degradation rate of the membrane. Joining such a study with the examination of carbon corrosion would be of great benefit, and the methodology presented here should provide a convenient starting point. Depending on the application of interest, appealing variations could be introduced by, for example, other CO concentrations or Pd-based catalysts.

In applications where the recirculation of the fuel is to be considered, thorough understanding of the poisoning dynamics is crucial. The outcomes of this thesis provide the ongoing research into PEMFCs at system level with an inspiring reference point.

References

[1] F. W. Ostwald, *Zeitschrift für Elektrotechnik und Elektrochemie* **1894**, *1*, 122–125.

[2] F. De Bruijn, V. Dam, G. Janssen, *Fuel Cells* **2008**, *8*, 3–22.

[3] X.-Z. Yuan, H. Li, S. Zhang, J. Martin, H. Wang, *Journal of Power Sources* **2011**, *196*, 9107–9116.

[4] I. Staffell, R. Green, *International Journal of Hydrogen Energy* **2012**.

[5] A. Bard, L. Faulkner, *Electrochemical methods: fundamentals and applications 2nd ed.*, John Wiley Sons, **1980**.

[6] J. Reitz, F. Milford, R. Christy, *Foundations of Electromagnetic Theory 4th ed.*, Addison Wesley, **1992**, 33-34.

[7] J. O. Bockris, A. K. N. Reddy, *Modern Electrochemistry 2B: Electrodics in Chemistry, Engineering, Biology, and Environmental Science 2nd ed.*, Kluwer Academic / Plenum, **2000**.

[8] A. Lutz, R. Larson, J. Keller, *International Journal of Hydrogen Energy* **2002**, *27*, 1103–1111.

[9] J. Larminie, A. Dicks, *Fuel Cell Systems Explained 2nd ed.*, John Wiley Sons, **2003**.

[10] M. M. Mench, *Fuel Cell Engines 1st ed.*, John Wiley Sons, **2008**.

[11] S. Wright, *Renewable energy* **2004**, *29*, 179–195.

[12] J. Hirschenhofer, D. Stauffer, R. Engleman, M. Klett, *Fuel cell handbook*, US Department of Energy, Office of Fossil Energy, Federal Energy Technology Center, **1998**.

[13] B. Smitha, S. Sridhar, A. Khan, *Journal of Membrane Science* **2005**, *259*, 10–26.

[14] F. Büchi, G. Scherer, *Journal of the Electrochemical Society* **2001**, *148*, A183–A188.

[15] W. Dai, H. Wang, X. Yuan, J. Martin, D. Yang, J. Qiao, J. Ma, *International Journal of Hydrogen Energy* **2009**, *34*, 9461–9478.

[16] F. Barbir, *PEM Fuel Cells: Theory and Practice 1st ed.*, Academic Press, **2005**, p. 89.

[17] A. Dicks, *Journal of Power Sources* **2006**, *156*, 128–141.

[18] S. Park, J.-W. Lee, B. N. Popov, *International Journal of Hydrogen Energy* **2012**, *37*, 5850–5865.

[19] N. Zamel, X. Li, *Progress in Energy and Combustion Science* **2011**, *37*, 292–329.

[20] N. Rajalakshmi, T. Jayanth, K. Dhathathreyan, *Fuel cells* **2004**, *3*, 177–180.

[21] F. A. Uribe, S. Gottesfeld, T. A. Zawodzinski, *Journal of the Electrochemical Society* **2002**, *149*, A293–A296.

[22] R. Mohtadi, W.-K. Lee, S. Cowan, J. Van Zee, M. Murthy, *Electrochemical and solid-state letters* **2003**, *6*, A272–A274.

[23] W. Shi, B. Yi, M. Hou, F. Jing, P. Ming, *Journal of power sources* **2007**, *165*, 814–818.

[24] F. De Bruijn, D. Papageorgopoulos, E. Sitters, G. Janssen, *Journal of Power Sources* **2002**, *110*, 117–124.

[25] S. Srinivasan, *Fuel cells: From Fundamentals to Applications 1st ed.*, Springer, **2006**.

[26] R. J. Bellows, E. P. Marucchi-Soos, D. T. Buckley, *Industrial & engineering chemistry research* **1996**, *35*, 1235–1242.

[27] S. Sircar, W. Waldron, M. Anand, M. Rao, *Hydrogen recovery by pressure swing adsorption integrated with adsorbent membranes*, **1998**, US Patent 5,753,010.

[28] Y.-W. You, D.-G. Lee, K.-Y. Yoon, D.-K. Moon, S. M. Kim, C.-H. Lee, *International Journal of Hydrogen Energy* **2012**, *37*, 18175–18186.

[29] S. Markov, P. Weaver, M. Seibert, *Applied biochemistry and biotechnology* **1997**, *63*, 577–584.

[30] E. J. Wolfrum, A. S. Watt, *Bioreactor design studies for a novel hydrogen-producing bacterium*, Proceedings of the 2001 DOE Hydrogen Program Review, **2001** NREL/CP-570-30535.

[31] O. Korotkikh, R. Farrauto, *Catalysis Today* **2000**, *62*, 249–254.

[32] A. Heinzel, B. Vogel, P. Hubner, *Journal of Power Sources* **2002**, *105*, 202 – 207.

[33] ISO/DIN 14687-2:2012, *Hydrogen fuel - Product specification - Part 2: Proton exchange membrane (PEM) fuel cell applications for road vehicles.*

[34] P. Stonehart, P. Ross, *Catalysis Reviews* **1975**, *12*, 1–35.

[35] H. Igarashi, T. Fujino, M. Watanabe, *Journal of Electroanalytical Chemistry* **1995**, *391*, 119 – 123.

[36] N. Zamel, X. Li, *International Journal of Hydrogen Energy* **2008**, *33*, 1335–1344.

[37] S. Gilman, *The Journal of Physical Chemistry* **1964**, *68*, 70–80.

[38] C. Campbell, G. Ertl, H. Kuipers, J. Segner, *The Journal of Chemical Physics* **1980**, *73*, 5862.

[39] H. Gasteiger, N. Markovic, P. Ross Jr, *The Journal of Physical Chemistry* **1995**, *99*, 8290–8301.

[40] S. Gottesfeld, J. Pafford, *Journal of the Electrochemical Society* **1988**, *135*, 2651–2652.

[41] W. Wang, *Journal of Power Sources* **2009**, *191*, 400–406.

[42] L.-Y. Sung, B.-J. Hwang, K.-L. Hsueh, F.-H. Tsau, *Journal of Power Sources* **2010**, *195*, 1630–1639.

[43] T. Tingelöf, L. Hedström, N. Holmström, P. Alvfors, G. Lindbergh, *International journal of hydrogen energy* **2008**, *33*, 2064–2072.

[44] Z. Jusys, J. Kaiser, R. Behm, *Journal of Electroanalytical Chemistry* **2003**, *554*, 427–437.

[45] V. Stamenkovic, B. Grgur, P. Ross, N. Markovic, *Journal of The Electrochemical Society* **2005**, *152*, A277–A282.

[46] T. Kinumoto, M. Inaba, Y. Nakayama, K. Ogata, R. Umebayashi, A. Tasaka, Y. Iriyama, T. Abe, Z. Ogumi, *Journal of power Sources* **2006**, *158*, 1222–1228.

[47] D. Curtin, R. Lousenberg, T. Henry, P. Tangeman, M. Tisack, *Journal of Power Sources* **2004**, *131*, 41–48.

[48] M. Inaba, M. Sugishita, J. Wada, K. Matsuzawa, H. Yamada, A. Tasaka, *Journal of Power Sources* **2008**, *178*, 699–705.

[49] B. Du, R. Pollard, J. Elter, *ECS Transactions* **2006**, *3*, 705–713.

[50] C.-H. Chen, C.-C. Chung, H.-H. Lin, Y.-Y. Yan, *Journal of fuel cell science and technology* **2008**, *5*.

[51] N. Markovic, B. Grgur, P. Ross, *The Journal of Physical Chemistry B* **1997**, *101*, 5405–5413.

[52] Y. Hashimasa, Y. Matsuda, M. Akai, *ECS Transactions* **2010**, *26*, 131–142.

[53] H. Gasteiger, S. Yan, *Journal of power sources* **2004**, *127*, 162–171.

[54] H. Gasteiger, N. Markovic, P. Ross Jr, E. Cairns, *The Journal of Physical Chemistry* **1994**, *98*, 617–625.

[55] W. Lin, T. Iwasita, W. Vielstich, *The Journal of Physical Chemistry B* **1999**, *103*, 3250–3257.

[56] C. Saravanan, B. Dunietz, N. Markovic, G. Somorjai, P. Ross, M. Head-Gordon, *Journal of Electroanalytical Chemistry* **2003**, *554*, 459–465.

[57] C. Chung, C. Chen, D. Weng, *Applied Thermal Engineering* **2009**, *29*, 2518–2526.

[58] R. Bashyam, P. He, S. Wessel, S. Knights, *ECS Transactions* **2011**, *41*, 837–844.

[59] E. Antolini, *Journal of Solid State Electrochemistry* **2011**, *15*, 455–472.

[60] E. Antolini, *Energy & Environmental Science* **2009**, *2*, 915–931.

[61] E. Antolini, S. C. Zignani, S. F. Santos, E. R. Gonzalez, *Electrochimica Acta* **2011**, *56*, 2299–2305.

[62] Y.-H. Cho, Y.-H. Cho, J. W. Lim, H.-Y. Park, N. Jung, M. Ahn, H. Choe, Y.-E. Sung, *International Journal of Hydrogen Energy* **2012**, *37*, 5884–5890.

[63] N. Markovic, C. Lucas, B. Grgur, P. Ross, *The Journal of Physical Chemistry B* **1999**, *103*, 9616–9623.

[64] J. Zhang, R. Datta, *Journal of The Electrochemical Society* **2002**, *149*, A1423–A1431.

[65] A. Thomason, T. Lalk, A. Appleby, *Journal of power sources* **2004**, *135*, 204–211.

[66] W. Adams, J. Blair, K. Bullock, C. Gardner, *Journal of power sources* **2005**, *145*, 55–61.

[67] L. Carrette, K. Friedrich, M. Huber, U. Stimming, *Phys. Chem. Chem. Phys.* **2000**, *3*, 320–324.

[68] S. Lee, S. Mukerjee, E. Ticianelli, J. McBreen, *Electrochimica Acta* **1999**, *44*, 3283–3293.

[69] J. Davies, R. Nielsen, L. Thomsen, I. Chorkendorff, A. Logadottir, Z. Lodziana, J. Nørskov, W. Li, B. Hammer, S. Longwitz, et al., *Fuel Cells* **2004**, *4*, 309–319.

[70] C. Yang, P. Costamagna, S. Srinivasan, J. Benziger, A. Bocarsly, *Journal of Power Sources* **2001**, *103*, 1–9.

[71] L. Xiao, H. Zhang, T. Jana, E. Scanlon, R. Chen, E. Choe, L. Ramanathan, S. Yu, B. Benicewicz, *Fuel Cells* **2005**, *5*, 287–295.

[72] B. Du, R. Pollard, J. F. Elter, M. Ramani in *Polymer electrolyte fuel cell durabilitys*, Springer, **2009**, pp. 341–366.

[73] Q. Li, R. He, J. Jensen, N. Bjerrum, *Fuel Cells* **2004**, *4*, 147–159.

[74] D. C. Seel, B. C. Benicewicz, L. Xiao, T. J. Schmidt in *Handbook of Fuel Cells – Fundamentals, Technology and Applications*, John Wiley Sons, **2009**, pp. 1–13.

[75] Y. Zhai, H. Zhang, Y. Zhang, D. Xing, *Journal of power sources* **2007**, *169*, 259–264.

[76] A. Chandan, M. Hattenberger, A. El-kharouf, S. Du, A. Dhir, V. Self, B. G. Pollet, A. Ingram, W. Bujalski, *Journal of Power Sources* **2013**, *231*, 264–278.

[77] L. Pérez, P. Koski, J. Ihonen, A. Mendes **2013**, (to be submitted).

[78] S. Auvinen, T. Tingelöf, J. K. Ihonen, J. Siivinen, M. Johansson, *ECS Transactions* **2009**, *25*, 1811–1821.

[79] F.-B. Weng, B.-S. Jou, C.-W. Li, A. Su, S.-H. Chan, *Journal of Power Sources* **2008**, *181*, 251–258.

[80] J. Stumper, S. A. Campbell, D. P. Wilkinson, M. C. Johnson, M. Davis, *Electrochimica Acta* **1998**, *43*, 3773–3783.

[81] L. Pérez, T. Rajala, J. Ihonen, P. Koski, J. Sousa, A. Mendes, *International Journal of Hydrogen Energy* **2013**, (to be published).

[82] G. Bender, M. Angelo, K. Bethune, S. Dorn, T. Thampan, R. Rocheleau, *Journal of Power Sources* **2009**, *193*, 713–722.

[83] D. Brett, P. Aguiar, N. Brandon, A. Kucernak, *International journal of hydrogen energy* **2007**, *32*, 863–871.

[84] C. Bonnet, L. Franck-Lacaze, S. Ronasi, S. Besse, F. Lapicque, *Chemical Engineering Science* **2010**, *65*, 3050–3058.

[85] S. M. M. Ehteshami, S. H. Chan, *Electrochimica Acta* **2013**.

[86] L. Gubler, G. G. Scherer, A. Wokaun, *Physical Chemistry Chemical Physics* **2001**, *3*, 325–329.
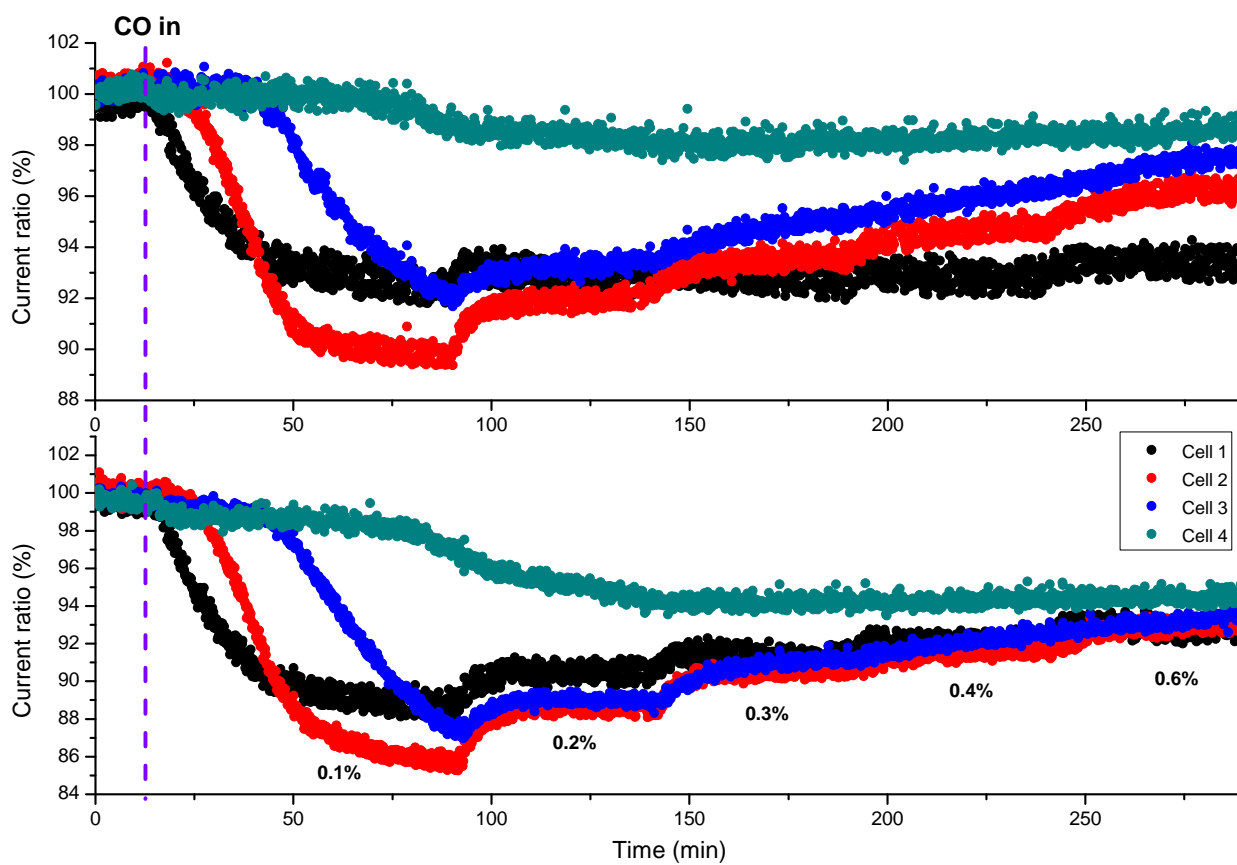
Appendix A

Figure 14: Current responses of experiments 2.3 (on top) and 2.4. Cell voltages were constant at 650 mV and 640 mV, respectively.
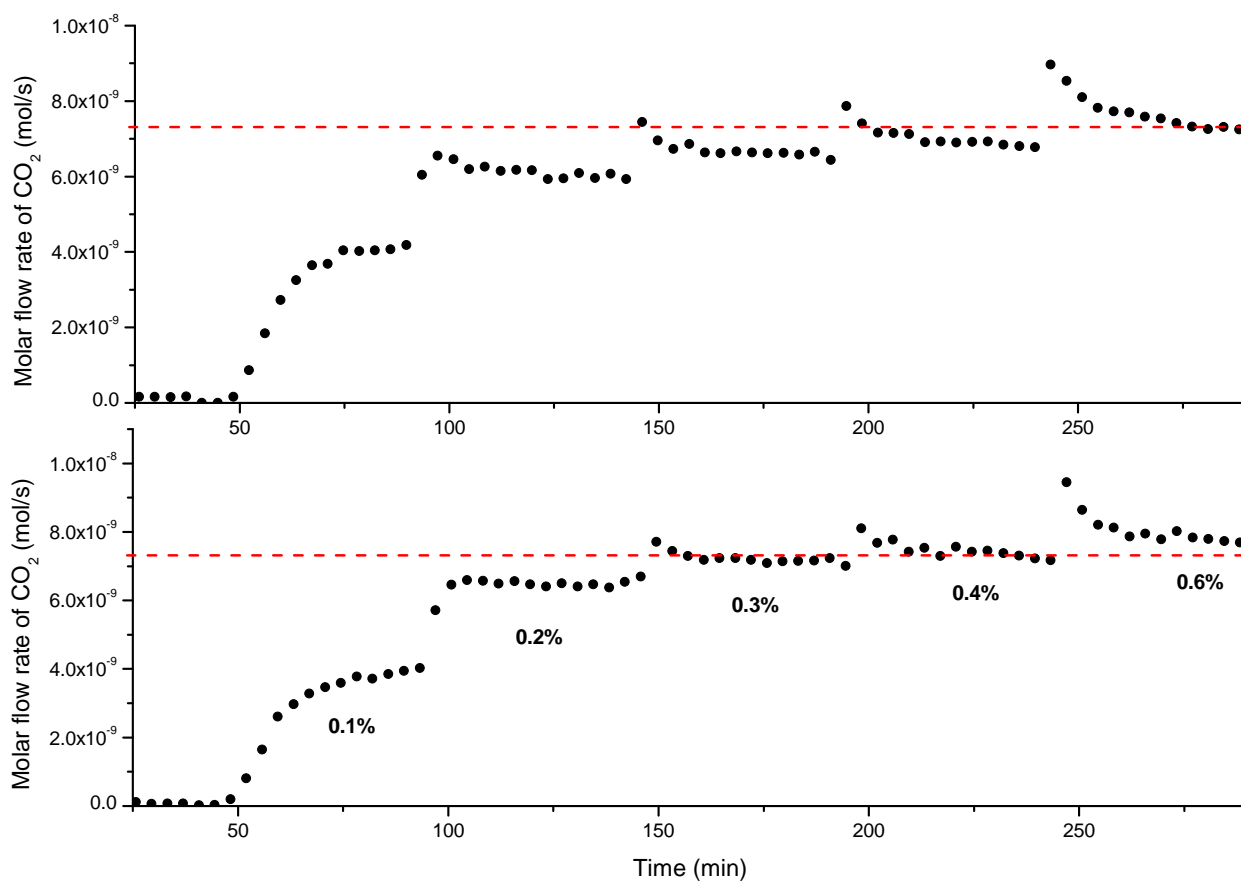
Figure 15: Molar flow rates of CO_2 at the anode outlet in experiments 2.3 (on top) and 2.4. The red dashed lines correspond to the molar flow of CO at the inlet.